

Department of Physics and Astronomy

University of Heidelberg

Master thesis

in Physics

submitted by

David Müller

born in Heidelberg

2017

Performance studies of irradiated scintillating fibre
modules and quality checks during serial
production for the
LHCb SciFi Tracker

This master thesis has been carried out by David Müller
at the
Physikalisches Institut
under the supervision of
Prof. Dr. Ulrich Uwer
and
Dr. Blake Leverington

Abstract:

The LHCb experiment will perform a detector upgrade during the LHC's Long Shutdown 2 in 2019 until 2020, allowing to collect up to 50 fb^{-1} of data. Due to the increased particle multiplicity, the downstream tracking system will be replaced by the Scintillating Fibre Tracker, which is composed of 6-layer mats of 2.42 m long scintillating fibres with a diameter of $250 \mu\text{m}$ and read-out by silicon photomultipliers.

To study the effect of the non-uniform radiation of the SciFi Tracker, test modules were irradiated at the CERN PS with the expected dose profile. The irradiated modules are investigated in the lab with a ^{90}Sr source as well as in a test beam with 180 GeV pions, protons and muons. Measurements of the reduced light yield and the detector performance will be presented along with additional measurements performed during the detector construction to ensure good quality of the fibre modules during serial production.

Kurzfassung:

Das LHCb Experiment wird ein Detektor-Upgrade während des LHC Long Shutdown 2 von 2019 bis 2020 durchführen. Dies ermöglicht bis zu 50 fb^{-1} an Daten zu sammeln. Aufgrund der höheren Okkupanz wird das Tracking System durch den Scintillating Fibre Tracker ersetzt. Dieser besteht aus 6-lagigen Matten aus 2,42 m langen szintillierenden Fasern mit einem Durchmesser von $250 \mu\text{m}$ welche mit Silizium-Photomultipliern ausgelesen werden.

Um den Effekt der ungleichmäßigen Strahlungs-Umgebung am SciFi Tracker zu untersuchen, wurden Test-Module mit der erwarteten Dosis der Laufzeit am CERN PS bestrahlt. Diese Module wurden sowohl im Labor mit einer ^{90}Sr Quelle als auch in einem Strahl Test mit 180 GeV Pionen, Protonen und Myonen untersucht. Messungen der verringerten Lichtausbeute und der Detektorperformance werden präsentiert. Ebenso wie auch zusätzliche Messungen während dem Detektorbau um eine gute Qualität der Faser-Module während der Serienproduktion zu garantieren.

Contents

1	Introduction	7
2	The LHCb Experiment	9
2.1	Physics at LHCb	9
2.1.1	Standard Model of Particle Physics	9
2.1.2	Search for Physics Beyond the SM	10
2.2	The LHCb Detector	11
2.2.1	Tracking Detectors	11
2.2.2	Particle Identification	13
2.2.3	Trigger System	14
2.3	LHCb Upgrade	14
3	The Scintillating Fibre Tracker	19
3.1	Requirements	19
3.2	Radiation Environment	20
3.3	Layout of the SciFi Detector	20
3.4	Scintillating Fibres	21
3.4.1	Plastic Scintillators	23
3.4.2	Attenuation	25
3.5	Fibre Mats and Modules	26
3.5.1	Fibre Mats	26
3.5.2	Fibre Modules	27
3.5.3	Light Injection	28
3.6	Silicon Photo Multipliers	29
3.6.1	Semiconductors	30
3.6.2	Avalanche Photodiode	32
3.6.3	Characterization	33
3.7	Clusterization	34
3.8	Readout Electronics	35
4	Test Stand for Fibre Mat Qualification	37
4.1	Motivation	37
4.2	Test Stand for Light Yield Measurements	37
4.2.1	Readout Electronics	38
4.2.2	Particle Trigger System	40
4.2.3	SiPM Calibration for Fibre Mat Read-Out	41
4.2.4	Particle Sources	43

4.3	Light Yield	44
5	Scintillating Fibre Radiation Damage	47
5.1	Introduction	47
5.2	Module Irradiation at CERN	48
5.2.1	Module Design	48
5.2.2	Irradiation Parameters	49
5.2.3	Previous Light Yield Measurements	50
5.3	Time Dependence of the Irradiation Effect	50
5.3.1	Initial Characterization	50
5.3.2	Characterization After Irradiation	52
5.3.3	Time Constant	54
5.4	Testing with Particle Beam	57
5.4.1	Test Beam Setup	57
5.4.2	Pre-Analysis & Track Reconstruction	58
5.4.3	Light Yield	59
5.4.4	Hit Efficiency	62
5.5	Summary	63
6	Quality Checks for Serial Production of Fibre Mats and Modules	67
6.1	Fibre Mats	67
6.1.1	Attenuation Length	67
6.1.2	Gain of the Mirror	68
6.1.3	Longitudinal Cut	68
6.2	Fibre Modules	73
6.3	Summary	74
7	Conclusion	77
I	Appendix	79
A	Bibliography	81

1 Introduction

The Standard Model (SM) of particle physics was developed during the second half of the 20th century. Ever since, it has explained almost every experimental observation in the field of particle physics. All known matter as well as their interactions are described by this theory. However, there are observations, like dark matter or neutrino oscillation, which cannot be explained by the SM. New theories with new phenomena are required to explain these observations.

The Large Hadron Collider (LHC), located at CERN¹ near Geneva, Switzerland, is the world's largest circular accelerator which provides the environment to test the SM and to search for new phenomena. The LHCb experiment, located at one of the interaction points of the LHC, is designed for high precision measurements of heavy flavour physics.

Currently, the limiting factor for most of the measurement uncertainties is statistics. Therefore, the LHCb detector will be upgraded during LHC's Long Shutdown 2 starting in 2018. While 3 fb^{-1} of the total integrated luminosity have been collected by now, the collaboration would like to collect 50-100 fb^{-1} until 2030. This upgrade allows to increase the current instantaneous luminosity by a factor of five to $\mathcal{L} = 2 \times 10^{33} \text{ cm}^{-2} \text{ s}^{-1}$. The current tracking system is a hybrid system containing a silicon-strip Inner Tracker around the beampipe and a straw drift tube Outer Tracker. Since the Outer Tracker will not be able to perform as well as required with the high particle multiplicities, the whole system will be replaced by a Scintillating Fibre Tracker (SciFi).

Scintillating fibres with a length of 2.42 m and a diameter of $250 \mu\text{m}$ are the sensitive component of the detector. The fibres are wound to six-layer fibre mats which are assembled to modules. The modules are arranged in twelve layers perpendicular to the beampipe covering an active region of around 326 m^2 . To provide the necessary granularity for a high spatial resolution and a fast response, the detector is read out by arrays of silicon photo multipliers (SiPM).

This thesis investigates the performance of irradiated SciFi test modules in a particle beam as well as quality checks before and during the serial production of the SciFi modules. It is structured as follows:

Chapter 2 starts with an introduction to the physics of LHCb, followed by a description of the current LHCb detector design and the planned upgraded detector. The SciFi Tracker itself is described in more detail in Chapter 3. After this introduction the experimental setup used to study different detector properties as well as a motivation is introduced in Chapter 4. Chapter 5 focusses on the irradiation of SciFi modules, the annealing after a short term irradiation to the expected lifetime dose

¹Conseil Européen pour la Recherche Nucléaire

and performance tests in a particle beam. In Chapter 6, different quality checks are described which have been done prior to and during the serial production. Finally a conclusion is given in Chapter 7.

2 The LHCb Experiment

The LHCb detector is one of the four main experiments at the Large Hadron Collider (LHC). The LHC, which is located at CERN (Conseil européenne pour la recherche nucléaire) near Geneva, is a 26.7 km long circular proton-ion collider. It is positioned at a depth of about 100m underground, as shown in Figure 2.1. Bunches of protons collide at the four main experiments [1]

- ALICE (A Large Ion Collider Experiment)
- ATLAS (A Toroidal LHC Apparatus)
- CMS (Compact Muon Solenoid)
- LHCb (Large Hadron Collider beauty)

with a centre of mass energy of $\sqrt{s} = 14$ TeV. The ATLAS and CMS experiments are build as multi-purpose detectors to study a variety of different phenomena, whereas ALICE and LHCb are more specialized. Not only is the LHCb experiment the smallest in size, the layout of the detector differs strongly from the other three main experiments. LHCb with its sub-detectors is described in more detail below.

2.1 Physics at LHCb

The LHCb experiment was developed for the indirect search for new physics in heavy flavour physics processes. It focusses on precision measurements of decay properties of hadrons which include bottom- (also called beauty-) or charm- quarks. The observation of unusual rates or decay distributions or the observation of unusually large CP violation could point to physics beyond the Standard Model.

2.1.1 Standard Model of Particle Physics

The Standard Model (SM) of particle physics is an effective quantum field theory which describes all known elementary particles as well as their interactions. The theory unifies three of the four main interactions: the electromagnetic force, the weak force and the strong force. The gravitational force is not included.

The elementary particles are divided in 12 spin-1/2 particles called fermions, four spin 1 gauge bosons and one spin-0 boson. The fermions are again divided in two groups, six quarks and six leptons which both exist in three generations. Quarks carry the so called color charge of the strong interaction and are named down (d), up (u), strange (s), charm (c), bottom (b) and top (t). The fermions are named

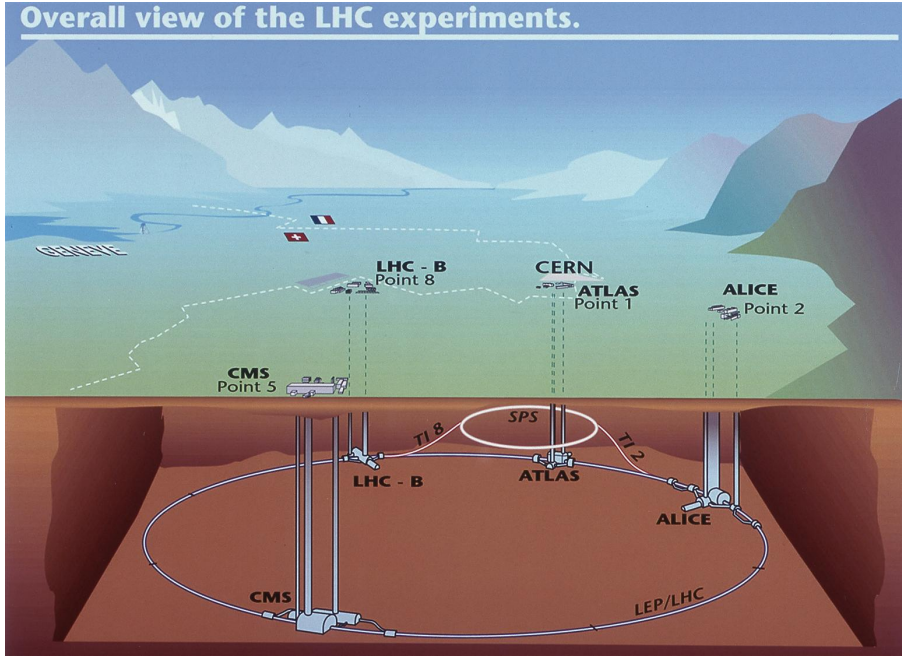


Figure 2.1: Overview of the LHC with the four main experiments ALICE, ATLAS, CMS and LHCb as well as the pre-accelerator ring (SPS). [2]

electron (e), muon (μ) and tau (τ) with a corresponding neutrino each (ν_e, ν_μ, ν_τ). Additionally each fermion has its own counterpart, an antiparticle, with same mass but opposite charge and quantum numbers. The carriers of the forces are the four spin-1 gauge bosons: photon (γ), two W-bosons (W^\pm), the Z-boson (Z^0) and the gluons (g). The latest discovery in particle physics was a Higgs-like, spin-0, particle predicted already in the 1960s. The so called Higgs-mechanism is responsible for the masses of the particles of the SM. All the particles are summarized in Figure 2.2. While leptons exist as free particles, quarks are always found in bound states, so called hadrons, of two or three quarks. These are called mesons and baryons respectively. But also exotic hadrons with more than three quarks are possible, like tetra- and penta-quark bound states.

2.1.2 Search for Physics Beyond the SM

The SM is a very successful theory where all measurements agree within uncertainties. But there are many observations which are not described by the Standard Model, for example gravitation, neutrino masses, dark energy and dark matter. Therefore the search for phenomena beyond the description of the SM is a major part of the research program of the LHC.

The LHCb experiment focusses on the decays containing a heavy charm or bottom quark and the indirect search for new effects. New effects can contribute to quantum loops which would modify the decay properties of the hadrons significantly.

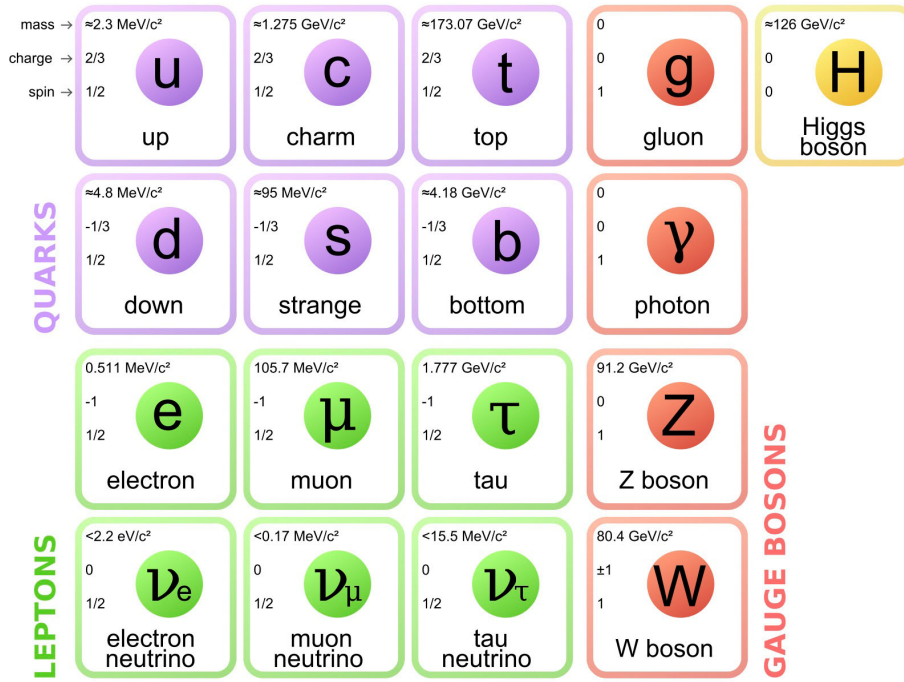


Figure 2.2: Standard Model of particle physics. [3]

Precise measurements of decay properties and their deviation from Standard Model predictions provide a sensitive test for new effects. Due to large production rates, the search for exotic hadron states with unusual quark content is also feasible with the LHCb experiment.

2.2 The LHCb Detector

Compared to the other three main experiments which cover a large fraction of the full solid angle, the LHCb detector is build as an single armed forward spectrometer which has an angular coverage of 10 mrad to 250-300 mrad. Since heavy flavour particles decaying predominately in forward and backward direction there is no need to cover the full solid angle. In order to keep down the costs only the forward direction is instrumented which reduces the amount of data by a factor of two. Figure 2.3 shows the cross section of the detector. It consist of two types of sub-detectors. One part are the tracking stations which are used for reconstruction of the tracks of charged particles to determine their vertices and momenta. Other detectors provide particle identification.

2.2.1 Tracking Detectors

Charged particle tracks are reconstructed using the Vertex Locator (VELO), the Tracker Turicensis (TT) and the tracking stations (T1-T3). The tracking stations

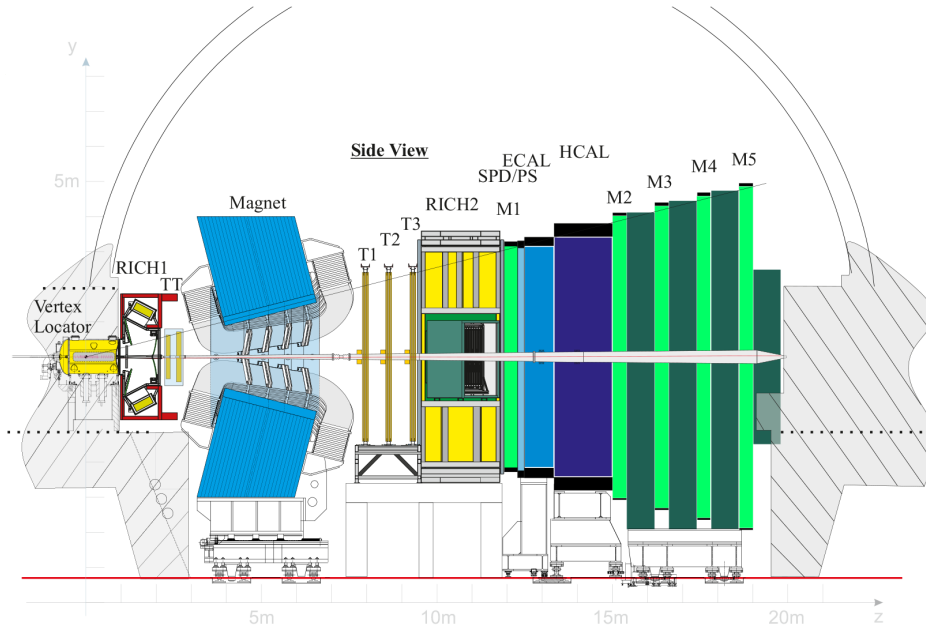


Figure 2.3: Schematic view of the current detector design of the LHCb experiment. [4]

consist of an Inner and an Outer Tracker (IT/OT) each. A large dipole magnet is placed between the TT and the tracking stations to deflect the particles. With the reconstructed tracks in front of and after the magnet the momentum of charged particles is determined.

Vertex Locator (VeLo). The VeLo is positioned directly at the point of collision and consists of 21 stations of silicon strip detectors. With a resolution in the transverse direction of $10 \mu\text{m}$ and a resolution of $40 \mu\text{m}$ along the beam axis, it reconstructs the primary vertex as well as the secondary decay vertices.

Tracker Turicensis (TT). The TT is the first of four parts of the tracking system and is positioned upstream of the dipole magnet. Each station consists of four layers where the middle two are tilted by $\pm 5^\circ$. The TT is made out of layers of silicon strip detectors with a resolution of $50 \mu\text{m}$. Due to the weak stray field of the magnet, also the momentum of low energy particles can be determined which are bent out of the detection area of the following tracking stations.

Tracking Stations (T1-T3). Directly behind the magnet the other 3 tracking stations (T1-T3) are located. Each of these consist of an Inner Tracker (IT) and an Outer Tracker (OT). The IT, like the TT, is made out of silicon strip detectors to cover the region around the beam pipe with an horizontal spatial resolution of 50

μm . The OT is a straw tube detector, which uses a mixture of Ar-CO₂-O₂ and has a resolution of 200 μm . The trajectories of charged particles are bent horizontally by a large dipole magnet with an integrated magnetic field of $\int Bdl = 4,2 \text{ Tm}$, which is placed between the TT and the T stations. The momentum is determined by the amount of bending.

2.2.2 Particle Identification

Besides detectors for tracking measurement, two RICH-detectors, a calorimeter system and muon stations are used for particle identification and energy measurements.

Ring Imaging Cherenkov Detector (RICH). A Ring-Imaging Cherenkov (RICH) detector is positioned between VELO and TT and also between the T stations and the calorimeter to perform particle identification (PID). They benefit from the phenomena that highly charged particles traveling through a material with a velocity greater than the speed of light in this material emit Cherenkov light. This light is emitted under a characteristic angle, $\cos(\theta) = \frac{1}{n\beta}$ with the relativistic velocity $\beta = \frac{v}{c}$ and the index of refraction n of the material. The measurement of this angle determines the velocity of the particle and together with the momentum information from the tracking system the particle mass can be obtained. The upstream RICH detector, RICH1, combines two radiators, silica aerogel (for momenta up to 10GeV/c) and C₄F₁₀ gas (for momenta up to 40 GeV/c) and covers an angular acceptance of 25-300 mrad. RICH2, which is located behind the dipole magnet and the T stations, has a CF₄ gas radiator (for momenta up to 100GeV/c) and covers an angular acceptance of 15-220 mrad.

Calorimeter System (SPD/PS/ECAL/HCAL). The first part of the calorimeter system is the Preshower Detector (PS) and the so called Scintillating Pad Detector (SPD) which is used to separate photons and electrons, since it is insensitive to neutral particles. Downstream of the SPD is a 12 mm thick lead plate to induce electromagnetic showers. Since hadrons produce only very little energy deposition in the thin lead sheet, it is used to separate these from electrons and photons. The energy measurement is performed in an electromagnetic (ECAL) and a hadronic (HCAL) calorimeter. Both are sampling calorimeters which consist of alternating layers of scintillators and absorber material. For the ECAL lead is used to absorb the particles whereas the HCAL uses iron for absorption. The particles induce electromagnetic or hadronic particle showers which are detected by the scintillating material.

Muon Stations (M1-M5). Each of the five muon stations (M1-M5) consist of multi-wire proportional counter (MWPC). The muon stations M2-M5 are interleaved by a 80 cm thick iron absorber. Due to the minimum ionizing properties only muons are able to pass the absorber material. The muon stations (M2-M5) are placed at

the end of the detector, only the first muon station (M1) is positioned in front of the calorimeter system. It is used for an improved muon momentum determination of the hardware muon trigger.

2.2.3 Trigger System

Since it is not possible to store the data of every collision at the collision rate of 40 MHz, potentially interesting events have to be filtered. Therefore a two level trigger system has been developed.

- The so called Level0-Trigger, a pure hardware trigger built out of electronic components, reduces the event rate to about 1MHz. It uses the information from the calorimeter system and the muon chambers to select either particles which have a high transverse energy in the calorimeter or which have a high transverse momentum in the muon chambers.
- The second level is called High Level Trigger (HLT), a pure software trigger which is again divided in two stages HLT1 and HLT2. HLT1 reduces the data rate to 50 kHz by performing a partial reconstruction in the VeLo and determining the position of the primary vertices in the event. HLT2 searches for secondary vertices and applies decay length and mass cuts which reduces the data rate to around 4.5 kHz.

2.3 LHCb Upgrade

Up to now 3 fb^{-1} of data have been collected, but most of the LHCb measurements remain statistically dominated. During the Long Shutdown 2 in 2018 the LHCb detector will be upgraded to have a trigger-less read-out of the full detector at 40 MHz event rate, removing the 1 MHz Level-0 trigger. This allows to feed complete events every 25 ns to the LHCb data acquisition farm so a full software analysis can be applied on each bunch crossing. The upgraded detector will increase the luminosity by a factor of five to $\mathcal{L} = 2 \times 10^{33} \text{ cm}^2\text{s}^{-1}$. After 10 years of operation a total of 50 fb^{-1} of data will be collected [5]. Additionally a new software trigger will improve the selection of interesting hadronic events.

Figure 2.4 shows a schematic of the upgraded detector design featuring the new Vertex Locator (VeLoPix), the Upstream Tracker (UT) and the Scintillating Fibre Tracker (SciFi) for tracking as well as two upgraded RICH detectors for particle identification and the calorimeter system for measuring the particle energy.

Vertex Locator (VeLoPix). The current VeLo detector will be replaced by a pixel system with electronics capable of reading out the full 40 MHz bunch crossing rate. The silicon pixel sensors will have the dimensions of $55 \times 55 \mu\text{m}^2$. Additionally the detector will be closer to the interaction region and have a reduced material budget. This leads to an improved track reconstruction performance and an overall

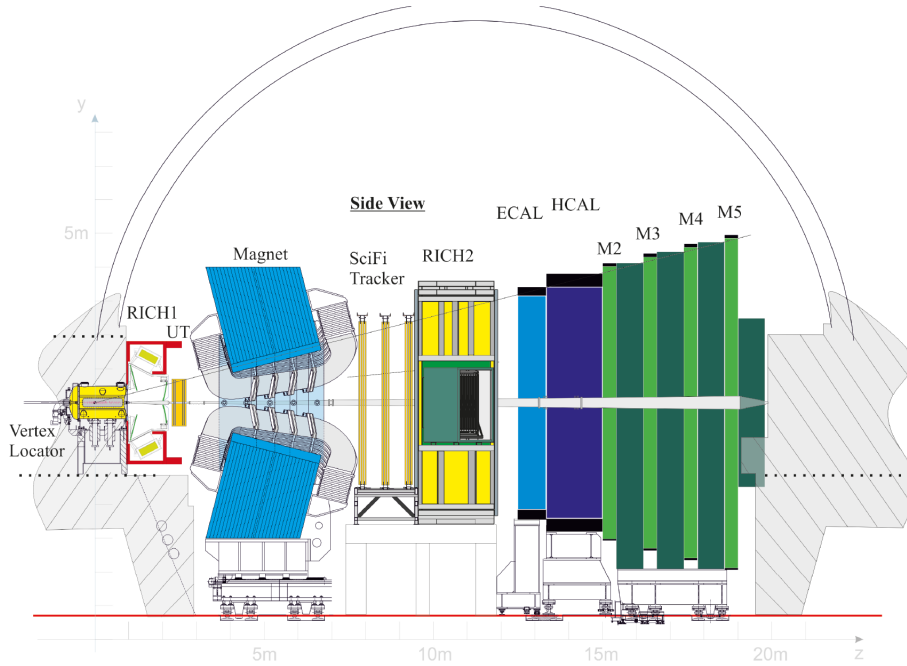


Figure 2.4: Schematic view of the upgraded detector design of the LHCb experiment. [4]

better resolution. The sensors will be read out by the VeloPix ASIC which is based on the Timepix3 ASIC with data-driven read-out [6]. As shown in Figure 2.5 the finished detector consists of two halves with 26 modules each aligned along the beam direction.

Upstream Tracker (UT). The four planes of the current TT will be replaced by four new silicon micro-strip planes which have an improved coverage of the LHCb acceptance. As shown in Figure 2.6 the micro-strip sensor are placed on so called "staves" which run vertically in the two outer layers and will be tilted by $\pm 5^\circ$ on the inner two layers. Depending on the distance from the beampipe, the staves consist of 14 or 16 sensors respectively. The so called SALT front-end ASIC will sit close to the sensors providing the required read-out rate of 40 MHz [4].

Scintillating Fibre Tracker (SciFi). The Scintillating Fibre Tracker will replace the IT and the OT with a single detector technology made of scintillating fibres. Chapter 3 will focus on a more detailed description of the new SciFi Tracker.

RICH. The geometric structure of both RICH detectors will remain unchanged. Since the current design would have a degraded PID performance at higher luminosity, some components will be changed. The optical arrangement will be redesigned to recover the PID performance loss due to the increase in occupancy. For the full

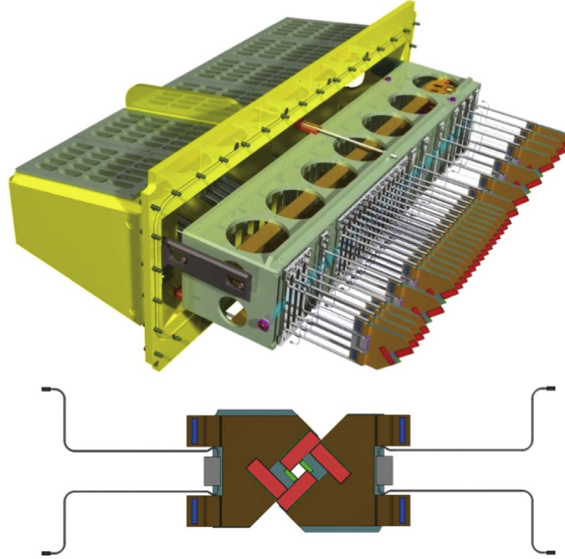


Figure 2.5: Schematic view of one half of the VeLoPix detector (top) and both detector halves closed (bottom). [6]

read-out at 40 MHz, it is required to replace the current Hybrid Photon Detectors (HPD) by multianode photomultipliers (MaPMT) with external read-out [7].

Calorimeter System. The biggest change in the Calorimeter will be the removal of the preshower detector PS/SPS and the lead converter since these detector parts are mainly used for the L0 Hardware Trigger. Likewise on the the other subdetectors, the read-out electronics will be replaced in order to be able to transmit data at the full LHC bunch crossing rate of 40MHz. Due to the faster aging of the PMTs at the five times higher luminosity, the gain of the PMTs will be reduced by a factor of five while increasing the sensitivity of the preamplifiers accordingly. The operation at higher luminosity does not require a replacement of the ECAL and HCAL modules as well as their photomultipliers [7].

Muon Stations. Due to the high particle multiplicities at the upgrade luminosity, the first muon station M1 will be removed during the upgrade. The correct association of M1 hits to the muon track segments would be not possible. Additionally M1 is not used for the muon identification algorithms. The layout of the remaining muon stations M2-M5 will not be modified. Due to the higher particle flux experienced by the innermost regions of M2, an additional shielding will be installed around the beampipe behind the calorimeter system. Since the read-out is already capable of the 40 MHz bunch crossing rate due to the current L0 muon trigger, no replacement is required. But the off-detector read-out electronics, which provides full hit information only at 1 MHz, has to be redesigned completely [7].

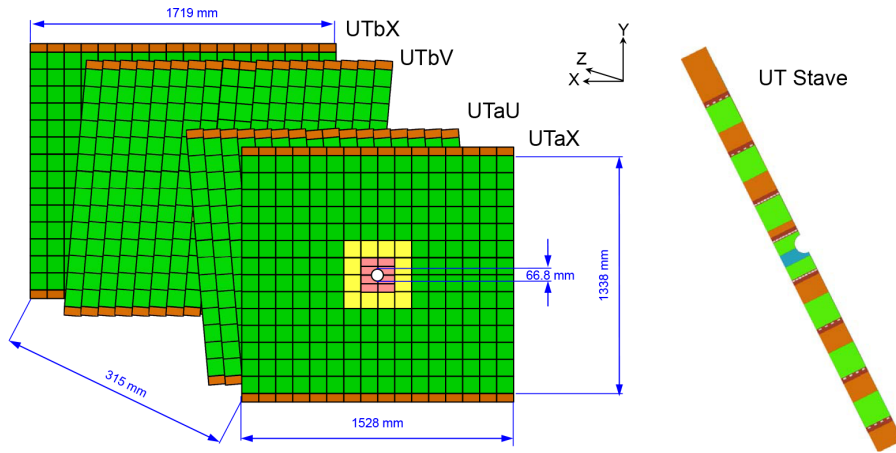


Figure 2.6: *Left*: Overview of the UT geometry with different sensor geometry indicated with colour. *Right*: Schematic of a UT Stave structure. Sensor are coloured green, flex cables brown and the ASICs in yellow. [4]

Trigger. As already mentioned above, the Hardware Level-0 trigger will be removed to be able to read out the detector at full LHC bunch crossing rate of 40 MHz. Instead there will be a software integrated low level trigger (LLT) which uses limited information from the calorimeters and the muon stations. Since this LLT is not necessary it will be kept as a backup solution to reduce the input rate to the software trigger by a factor of two. Afterwards a full track reconstruction, with an precision very close to the full offline reconstruction, will reconstruct particle tracks. A trigger selection is performed to reduce the output rate such that it can be processed by the offline computing [8]. The much increased band width and a higher trigger efficiency for hadronic B decays will increase the overall efficiency to detect and reconstruct hadronic B decays.

3 The Scintillating Fibre Tracker

During the LHC Long Shutdown 2 (LS2), starting in the end of 2018 and lasting until the end of 2020, the upgrade of the LHCb detector will take place. This upgrade will allow LHCb to run at a higher luminosity of $\mathcal{L} = 2 * 10^{33} \text{ cm}^2 \text{ s}^{-1}$ and to collect up to 50 fb^{-1} of data. The current downstream tracker, which consists of the silicon strip Inner Tracker and the straw tube Outer Tracker, will be replaced by a high granular, uniform, low-mass Scintillating Fibre Tracker (SciFi). Additionally the read-out of the front-end electronics will be a 40 MHz triggerless read-out. A schematic of the upgraded detector design is shown in Figure 2.4.

3.1 Requirements

In general, the SciFi Tracker should continue the tracks found in the upstream tracking stations. In addition it should provide a standalone particle track reconstruction for particles without a track in the upstream detectors. The following list shows the main requirements for the new SciFi detector [9]:

- The hit efficiency for single hits or clusters should be close to 99%.
- At any position of the detector, the accepted dark count rate (DCR) should be below 10% of the signal rate.
- The read-out rate of the detector should be 40 MHz with no dead time for digitization.
- The required spatial resolution in the bending plane (x direction) should be less than $100 \mu\text{m}$ whereas the required resolution in the vertical (y direction) should be about 1 mm.
- A precise alignment of the detector modules is necessary to achieve the spatial resolution. Therefore the construction principle of mats and modules has to assure that the fibres inside are straight and aligned better than $50 \mu\text{m}$ in x-direction and are flat within $300 \mu\text{m}$ in z-direction.
- To minimize the effect of multiple scattering the material budget in the acceptance region should be minimalized. The radiation length of a SciFi detection layer should not exceed 1% of X_0 .
- The required performance should be ensured up to an integrated luminosity of 50 fb^{-1} . The total ionizing dose around the beampipe will be 35kGy which

will change the transparency of the scintillating fibres and decrease the attenuation length. Additionally the SiPMs mounted on the outside will have seen a neutron fluence of up to 9.5×10^{11} neutron (1 MeV equivalent) / cm^2 which will increase their dark count rate significantly [10].

3.2 Radiation Environment

To estimate the radiation level at the tracking stations, a FLUKA [11, 12] simulation of the LHCb detector was performed, assuming an integrated luminosity of 50 fb^{-1} , a proton-proton cross-section of 100 mb and the detector geometry for the expected upgrade conditions at $\sqrt{s} = 14 \text{ TeV}$. For more details refer to reference [10]. This radiation environment will have an effect on the scintillating fibres as well as the silicon photo multipliers.

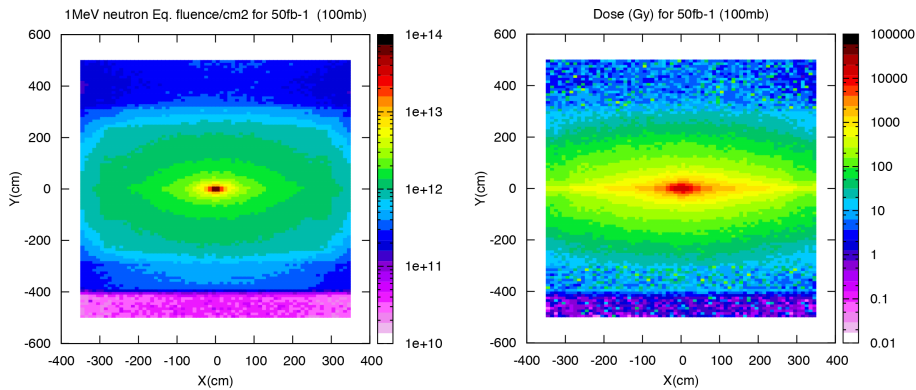


Figure 3.1: The expected 1 MeV neutron equivalent fluence per cm^2 (left) and the expected dose in the x-y plane (right) at T1 ($z = 783 \text{ cm}$) after an integrated luminosity of 50 fb^{-1} . [10]

Figure 3.1 shows the estimated 1 MeV neutron-equivalent fluence as well as the estimated ionizing dose at the first tracking station T1. The neutron fluence, plotted on the left side, in the readout region ($y = \pm 250 \text{ cm}$) is peaking at 9.5×10^{11} neutron (1 MeV equivalent) / cm^2 . The right side of Figure 3.1 shows the expected dose due to ionizing particles at T1. Since it is very inhomogeneous and follows roughly an $1/r^2$ distribution, it peaks at around 35 kGy around the beampipe and decreases to approximately 40 Gy in the readout region. Based on the simulated radiation profile two single fibre mat test modules were irradiated at the PS irradiation facility at CERN (more details in Chapter 5).

3.3 Layout of the SciFi Detector

The SciFi Tracker will use a single detector technology to cover an area of approximately $5 \times 6 \text{ m}^2$. It will have three stations (T1, T2, T3) with four detection layers

each. Two of the four layers have a stereo angle of $\pm 5^\circ$ of the fibres providing some spatial resolution in vertical direction. In T1 and T2 these layers each consist of 10 modules while T3 consists of 12 modules which are composed of eight fibre mats each. The two central modules in each layer have a squared cut out for the beampipe. The modules have the dimensions of $4.85 \text{ m} \times 0.528 \text{ m}$. Each fibre mat has a mirrored side and a read-out side where the Readout-Boxes (ROB) containing the silicon photo multipliers, front-end electronics and cooling will be mounted. The mats are glued into the module such that the mirrored side is at the centre of the module. In total there will be 128 modules covering an active region of around 326 m^2 . The fibre modules are then mounted on a frame for stability and cable management, which can be moved. Figure 3.2 shows a schematic view of the detector stations.

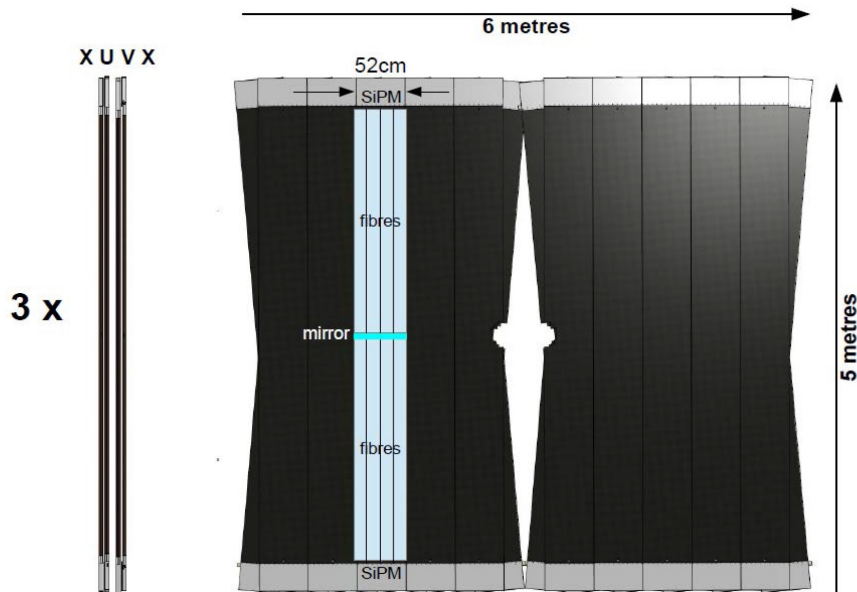


Figure 3.2: Schematic view of one of the planned SciFi Tracker stations. Each station consists of four planes while the outer planes have vertical (x) and the inner ones have a $\pm 5^\circ$ rotated (u,v) orientation. The final version will have a squared cut out for the beampipe. [9]

3.4 Scintillating Fibres

Scintillating plastic that is extruded into a fibre is the core material for scintillating fibres. It is surrounded by one or two claddings of non-scintillating material. These claddings have a lower refractive index and have a thickness of at least multiple wavelengths. Ionizing particles passing through the core of the fibre produce scintillation light which undergoes total internal reflection at the core-cladding boundary and propagate along the fibre.

Since plastic scintillating fibres have a fast response time they are widely used in particle detectors. They can be produced in different diameters with different properties and with different emission dopants. Depending on the dopants added, the emitting wavelength of the light can be shifted to increase the output at the end of the fibre. The response time of the fibre and the resistance to radiation damage is affected as well. The light propagation inside the fibre is dependent on the optical transparency, on impurities of the fibre, on density variations as well as on the boundary between the core and the claddings.

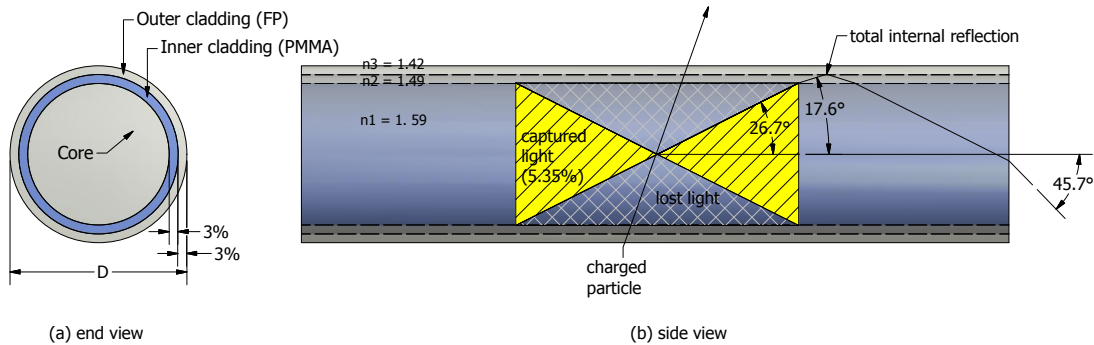


Figure 3.3: Schematic of a fibre consisting of the core and two layers of cladding as (a) end view and (b) side view. The light produced in the core material propagates through total internal reflection. [9]

As shown in Figure 3.3, only the light emitted within the cone in the direction of the detector will be observed. The light cone is defined by the interface between the core and the cladding. By using multiple claddings the amount of light which undergoes total internal reflection is increased. To increase the light yield, the light propagating in the opposite direction is reflected by a mirror which is glued on the fibre end.

The scintillating fibres used for the LHCb Upgrade Scifi Tracker have a diameter of $250 \mu\text{m}$ and are produced by Kuraray [13]. The two cladding layers have a nominal thickness of 3% each. The polystyrene core has a refractive index of $n = 1.59$ while both claddings have lower, decreasing index of refraction. The inner cladding is made out of polymethylmethacrylate (PMMA) with $n = 1.49$ while the outer one is made out of fluorinated PMMA (FP) with $n = 1.42$. The trapping efficiency of the scintillation light in the fibre is at least 5.35%. The decay time of the scintillation light is 2.8 ns and the light yield is expected to be around 8000 photons/MeV or 1600 photons per mm of scintillating fibre. [14]. Due to the efficiencies of light collection and transport, the amount of light detected at the end of the fibre is typically two magnitudes lower. For a minimum ionizing particle (MIP) one observes typically 15 - 20 photoelectrons per mm of scintillating fibre near the source as seen by a SiPM [14].

3.4.1 Plastic Scintillators

The energy loss of an ionizing particle, like a photon, electron or ion, leads to an excitation of a molecule, which decays and emits a photon, is called scintillation. This process is similar to luminescence where only a photon is absorbed. Three different processes of luminescence can occur: fluorescence, phosphorescence and delayed fluorescence, while fluorescence is the dominant process.

In fluorescence a photon is absorbed, leading to an excitation of an electron to a higher energy state. As shown in Figure 3.4, this excited S_3 state relaxes radiationless to the lowest excited singlet state S_{10} via internal conversion within 10^{-11} s. By decaying to any of the singlet ground states S_{00} , S_{01} etc., a photon of lower energy is emitted. The spectrum of luminescence depends on the ground state at which it is reabsorbed. This leads to a shift of the peak of the emission spectrum to a longer wavelength compared to the peak of the absorption spectrum. The emission spectrum is also independent of the wavelength of the absorbed photon. Due to an overlap in absorption and emission spectrum, the emitted photons can be reabsorbed by another molecule which leads to a decrease in observed fluorescence light.

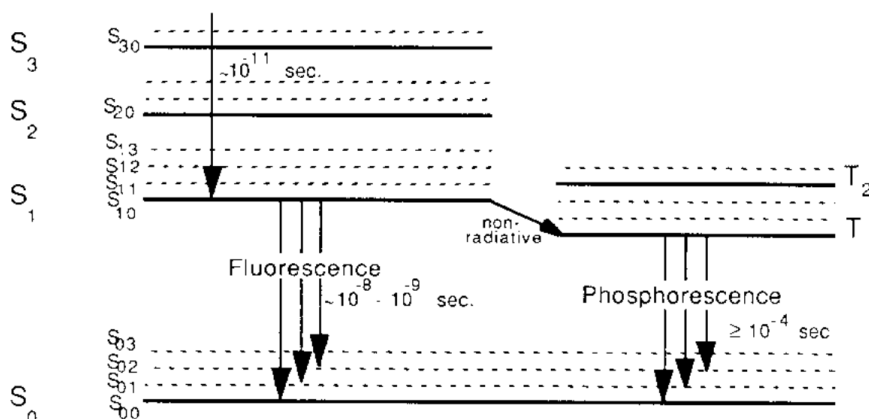


Figure 3.4: Jablonski diagram showing the decay scheme for fluorescence and phosphorescence. [15]

The process of scintillation has the same spectrum as fluorescence. Scintillation occurs mostly in aromatic organic materials which are plastics containing a benzene ring in the polymer chain. Benzene is a ring of six carbon atoms each bonded to a hydrogen atom. Two different types of bonds between the carbon atoms exist: σ - and π - bonds. While the σ -bonds are static, single electrons between the carbon atoms, the π -bonds are delocalized p-electrons. They are free to move around the ring and are not fixed to a carbon atom. These p-electrons are responsible for the scintillation [15]. Incident radiation can excite or liberate the p-electrons, but only

the excitation will lead to luminescence.

To increase the typically low quantum yield of pure polystyrene and shift the wavelength of the emission spectrum, two dopants are added to the core. However the quantum yield, which describes the ratio between emitted and absorbed photons, is still rather low, typically 5% [16]. Since the concentration of the dopants is very low, 1% by weight, only the base material can be considered to be excited by radiation [15].

Figure 3.5 shows the decay scheme of a base material, denoted with X, with two dopants, Y and Z. The excited electron first relaxes again radiation-less to a lower excited state in the base material X. From here it can decay via two competing routes. First, as described above it can decay non-radiative to a ground state of X. The second possibility is that the energy is transferred to the first dopant Y, either radiatively or non-radiatively. If the transfer occurs radiatively, the photon emitted by the decay of the excited state in X is reabsorbed by the dopant Y, which leads to an excited singlet state in Y with a lower energy than in X. Therefore the emission spectrum of X and absorption spectrum of Y have to overlap. Since this transition is rather slow, within 10^{-8} s, the dominant energy transfer is non-radiative, occurring within 10^{-12} s [15]. The Förster mechanism is responsible for this transition, where dipole-dipole interactions between molecules of the base material and the dopant transfer the energy [17].

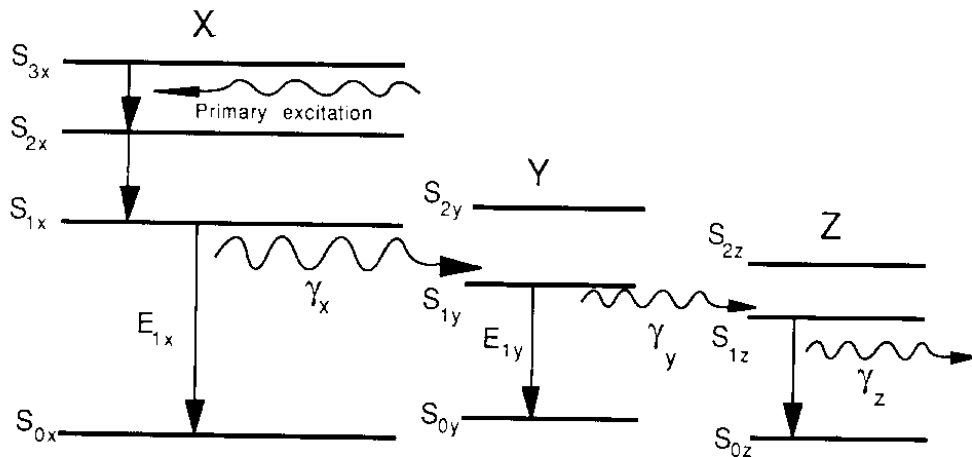


Figure 3.5: Decay scheme for plastic scintillator with two dopants. [15]

The second dopant is chosen such that the overlap between emission and absorption spectrum is minimized to minimize the re-absorption. The energy transfer between the two dopants Y and Z can occur also radiative or non-radiative. This depends on the concentration of the second dopant and the overlap between emission and absorption spectrum.

The dopants used in the LHCb scintillating fibres are p-Terphenyl and tetraphenyl-

butadiene (TBP). Figure 3.6 shows the different absorption (*red*) and emission (*blue*) spectra for the various compounds.

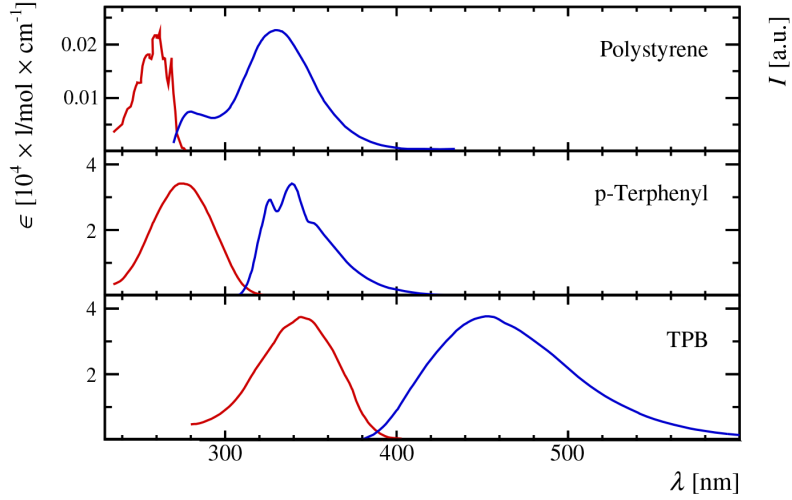


Figure 3.6: Absorption (red) and emission (blue) spectra for the different constituents of the LHCb scintillating fibres. The decadic molar attenuation coefficient for absorption and the intensity for the emission is shown. [4] (modified)

3.4.2 Attenuation

The light is attenuated when traveling through the fibre due to self-absorption and scattering. Scattering is mostly caused by imperfections and impurities inside the scintillator. A simplified model of the attenuation of the light is given by [18]:

$$I(x) = I_0 \cdot \exp\left(-\frac{x}{\Lambda}\right),$$

where $I(x)$ is the intensity at a distance x from excitation, I_0 is the intensity of light at the point of excitation and Λ is the attenuation length. The length at which the intensity drops to $1/e$ of the initial value is defined as the attenuation length.

The overlap of emission and absorption spectra is causing the self-absorption in scintillators. Photons with shorter wavelength are self-absorbed since they overlapping the absorption spectrum. Therefore the second dopant is added to the scintillator as a wavelength shifter in order to minimize the overlap. The simplified model can be modified to include this wavelength dependence:

$$I(x, \lambda) = I_0(\lambda) \cdot \exp\left(-\frac{x}{\Lambda(\lambda)}\right),$$

where $\Lambda(\lambda)$ is now the wavelength dependent attenuation length.

Not only self-absorption can reduce the light yield, also scattering on molecules in

the plastic can reduce it. This can deflect the photons from their path such that they do not longer undergo total internal reflection. The amount of scattering is not only wavelength dependent, it also depends on the size of the scattering particles. If these are smaller than the wavelength of the light, Rayleigh scattering happens where all light will be scattered off at the same frequency [19]. Whereas it will be scattered at many different frequencies when the size is similar or bigger. Since the Rayleigh scattering cross section is proportional to λ^{-4} , it is wavelength dependent and photons with shorter wavelength will be more strongly scattered [20].

A model of the propagation of light in a fibre shows, that two modes of attenuation exist [21]. One mode corresponding to rays of light traveling parallel to the fibre axis, called meridional rays. They passing through the fibre centre between each total internal reflection and are attenuated over long distances (long component). The second mode are non-meridional light rays, which are skewed relative to the fibre axis and are attenuated over shorter distances (short component). The attenuation depends on the angle γ between the projection of the light ray on a plane perpendicular to the axis of the fibre and the axis itself. For meridional rays, $\gamma = 0$, which leads back to the simplified model. If the angle is smaller than the critical angle θ_C , also the non-meridional light will undergo total internal reflection. Only if $\gamma > \theta_C$ the light rays are less likely to propagate.

To better model the propagation of light, a double exponential is used [18]:

$$I(x) = I_0 \left(\exp\left(-\frac{x}{\Lambda_L}\right) + \gamma \exp\left(-\frac{x}{\Lambda_S}\right) \right),$$

where Λ_L and Λ_S are the long- and short-components of the attenuation length, and γ is the relative strength of the two components.

3.5 Fibre Mats and Modules

3.5.1 Fibre Mats

To produce sufficient light yield at the photodetector, the scintillating fibre is wound to multi-layer mats with 6 staggered layers of fibres. In total around 8 km of scintillating fibre is used for one single fibre mat. To achieve a precise alignment of the single fibres a threaded winding wheel with a diameter of approximately 82 cm is used. While turning the wheel the fibres are guided into the grooves on the wheel with a pitch of 275 μm creating the first layer of the mat. The following five layers are wound such that the fibre is guided into the grooves between the fibres of the previous layer. This results in a homogenous fibre matrix as shown in Figure 3.7. The top schematic shows a fibre mat before performing a longitudinal cut. On the bottom two adjacent mats were drawn after the mats have been cut to a width of 130.45 mm. Additionally 9 pin holes are put in the central groove on the winding wheel. During the winding process these are filled with glue, making up precise alignment pins for the following production steps. A photograph of the serial

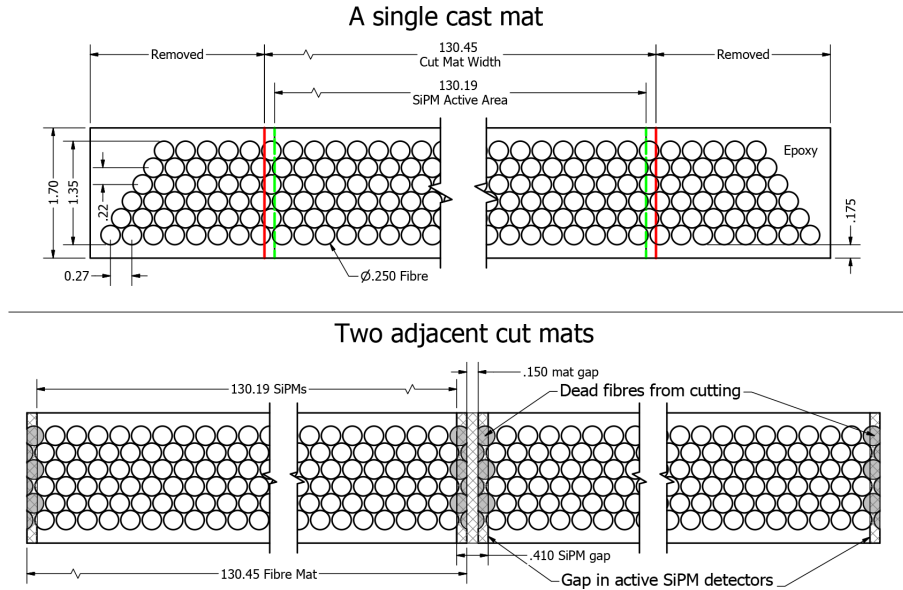


Figure 3.7: Schematic view of the cross-section of a single cast mat (top) and two adjacent cut mats (bottom). [4]

production mat winding setup is shown in Figure 3.8. At the end of the winding process a black foil is laminated on top of the top fibre layer to add stability and protection. After unforming the mat from the wheel a second black foil is glued on the pin side for light tightness. Afterwards, polycarbonate pieces are glued on the read-out side of the mat which are used for aligning the fibre mats in the following module production process as well as precisely aligning the SiPMs to the fibre mat. At the end, the foil cast mat is cut to the right length. To increase the light yield of the fibres an aluminized mylar foil mirror is attached on one side as the last production step in the winding centres.

Several constraints define the geometry of the fibre mats. Due to handling and production, the width of each fibre mat was chosen such that four 128 channel SiPM arrays can be placed. Including tolerances, this corresponds to a width of 130.45 mm with 130.19 mm of active fibre mat matching the active region of the SiPM arrays and 0.125 mm of dead fibre on each edge due to the longitudinal cutting. To cover the acceptance of the LHCb detector, 4,85 m in height, the length of the mat is required to be half this height including a 2 mm gap in between for production tolerances. This results in a length of the finished mat of 2,424 m. The total amount of fibre mats needed for the SciFi Tracker is 1024 which end up in 128 modules [9].

3.5.2 Fibre Modules

Since the fibre mats themselves are not stiff objects they are sandwiches between two 2 cm high honeycomb cores with a single carbon-fibre reinforced polymer skin on both sides. A SciFi fibre module consist of eight finished fibre mats, four aluminium

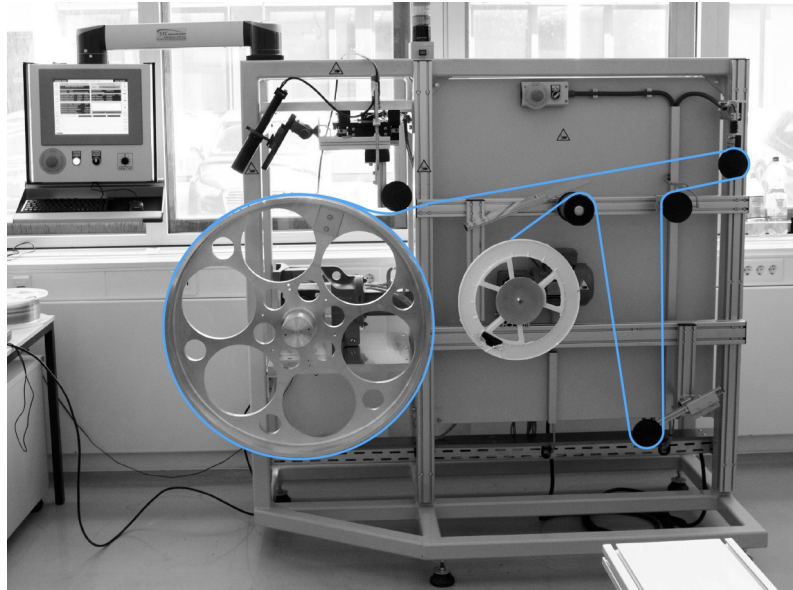


Figure 3.8: Picture of the mat winding setup for serial production. The blue lines show the path of the scintillating fibre beginning at the smaller spool through some small tension controlling wheels to the larger grooved winding wheel. [9]

endplugs, which provide mounting holes for read-out and alignment, two half-panels made from honeycomb core as well as two carbon-fibre sidewalls. Figure 3.9 shows a schematic view of the single module components.

For the assembly of a full size fibre module a template, machined from a single aluminium plate is used to assure precise alignment. The template consist of four rows of grooves to guide the alignment pins of the fibre mats in the right position. The aluminium endplugs are separated in two types, one containing the light injection system for the SiPM gain calibration, and one containing the mechanics for mounting and aligning the module to a large frame. Additionally the aluminium endplugs are part of the interface to the Readout-Boxes and have to be sealed to make it light tight. To provide strength and stiffness two half-panels are placed on each side of the entire module. To minimize the material budget of the detector a honeycomb-core is chosen.

3.5.3 Light Injection

The light injection system is used to calibrate the gain of the SiPMs and is implemented into the aluminium endplug of the module. It is required to achieve a uniform distribution of 2-10 photons across all 512 SiPM channels. The light-injection consists of a single optical fibre which is glued into an aluminium bar as shown in Figure 3.10. The surface of the fibre is scratched on the top allowing light to exit the fibre sideways. The light is produced by a VCSEL diode (vertical-cavity

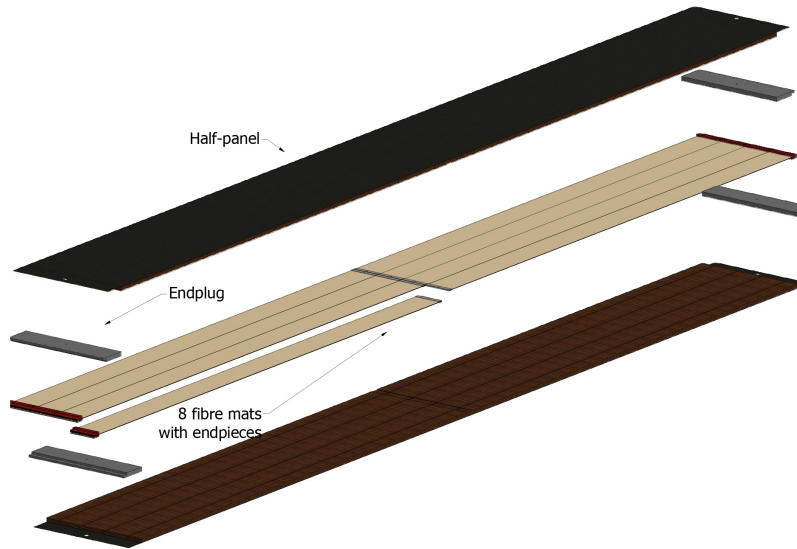


Figure 3.9: Schematic of a fibre module consisting of eight fibre mats, four endplugs and two half-panels. The two carbon-fibre sidewalls, which cover the edges of the module are not shown here. [9]

surface-emitting-laser) and routed through the optical fibre into the polycarbonate endpieces of the fibre mat and the fibres itself.



Figure 3.10: Picture of a lightbar with the optical fibre glued into an aluminium bar.

3.6 Silicon Photo Multipliers

To detect the photons created by the scintillating fibres, arrays of silicon photo multiplier (SiPM) are used. Multiple SiPM arrays are sitting on the read-out side of the fibre modules, which consist of 128 channels each. Each array is divided into two dies with 64 channels and a small gap of $220 \mu\text{m}$. Each channel has 104 pixel

with a pixel size of $62.5 \times 57.5 \mu\text{m}^2$ which leads to a channel size of $250 \times 1620 \mu\text{m}^2$ [22]. Figure 3.11 shows a picture of the central part of a SiPM array.

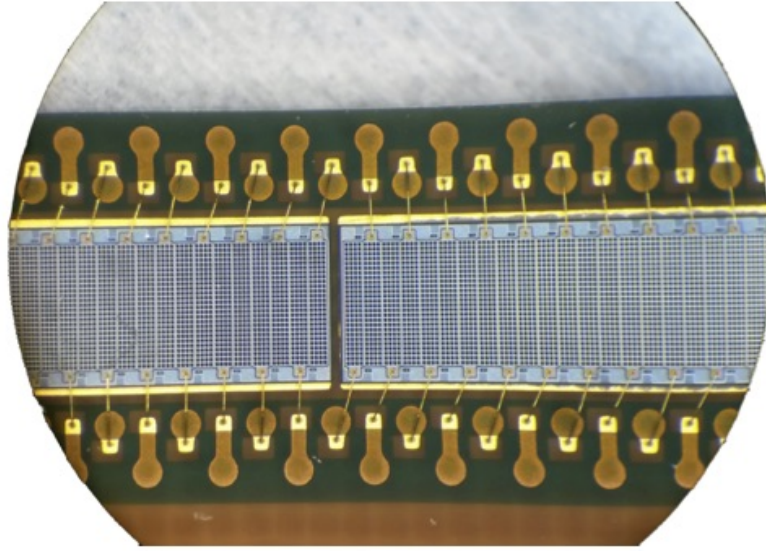


Figure 3.11: Microscopic picture of the central channels of an SiPM array with two 64 channel dies and a small gap in between. [22]

3.6.1 Semiconductors

Concerning their conductivity, solid materials can be categorized in three groups depending on the energy gap (E_g) between the upper boundary of the electron valence band (E_V) and the lower boundary of the electron conduction band (E_C) as shown in Figure 3.12.

- **Insulators** have an energy gap in order of a few eV which strongly suppresses the probability to thermally excite electrons from the valence band into the conduction band. The Fermi energy (E_F), which is defined as the energy up to which the bands are filled up at a temperature of 0 K, lies in between valence and conduction band.
- **Semiconductors** have a smaller energy gap between valence and conduction band which is in order of 1 eV. This gap is small enough to allow electrons to be thermally excited from the valence band to the conduction band.
- **Conductors** or metals have either overlapping bands or the Fermi level is sitting inside one of the bands.

Semiconductors again can be divided into two types, the intrinsic semiconductors and the doped semiconductors. **Intrinsic** semiconductors (type I) have an equal

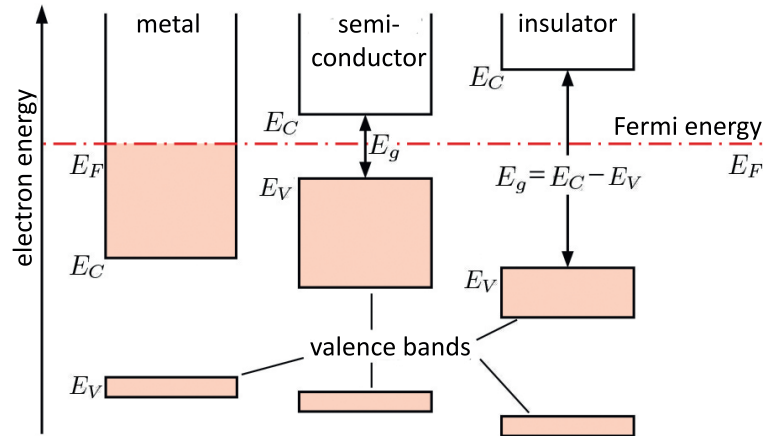


Figure 3.12: Schematic of the energy levels of the three groups of solid materials: metals, semi-conductors and insulators. [23] (modified)

density of electrons in the conduction band and missing electrons (holes) in the valence band. They are denoted with n for negative and p for positive charge carriers. Silicon (Si) and germanium (Ge) are typical intrinsic semiconductors. **Doped** semiconductors (type II) consist of an intrinsic semiconductor combined with a second material, the so called dopand which introduce impurities into the pure crystal. This leads to an unequal amount of charge carriers in both bands. Depending on the material added two types of doped semiconductors can be found:

- **n-type:** The dopand, called donor, has more electrons in its outer shell. Typical donors are phosphor (P) and arsenic (As).
- **p-type:** The dopand, called acceptor, has less electrons in its outer shell. Typical acceptors are aluminium (Al), indium (In) or gallium (Ga).

The dopants are chosen such that the energy level of the donors is close to the conduction band, whereas the energy level of the acceptors is close to the valence band. Since the number of both types of charge carriers differ due to the doping, the Fermi energy changes as well.

p-n-junction. By bringing a p-type and a n-type semiconductor in contact a so called p-n-junction is created. Since the Fermi levels of both regions equalizes in thermal equilibrium, the conduction and valence bands of both regions are shifted. This leads to a diffusion current with movements of free electrons from the n- to the p-type region, where they recombine with holes or are captured by acceptors, whereas the holes move from the p- to the n-type region, where they recombine with electrons or are captured by donators. Afterwards the boundary region, called depletion region, has no free charge carriers left. The electric field induces a drift

current which has the opposite direction to the diffusion current. An equilibrium state is generated with the potential U_D between n- and p-doped region:

$$eU_D = \Delta E_{\text{pot}} = E_C^p - E_C^n = E_V^p - E_V^n$$

with E_C and E_V the energy levels of conduction and valence band respectively. By applying an external voltage (U_{BIAS}), the p-n-junction works as a diode. Depending on the sign of the voltage the diode operates in two different bias modes. As shown in Figure 3.13 the resistance in the *forward bias* mode is almost negligible, whereas in the *reversed bias* mode a current will only flow when the voltage is larger than a specific breakdown voltage (U_{BD}). Since electrons have a chance to tunnel from valence to the conduction band a small leakage current flows below the breakdown voltage in the reversed bias mode.

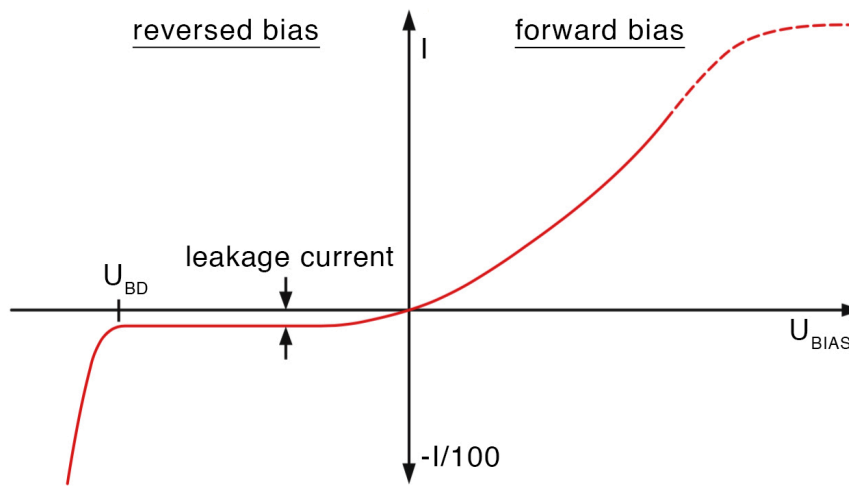


Figure 3.13: Diode current as a function of the applied bias voltage. [23] (modified)

3.6.2 Avalanche Photodiode

Each of the pixel of the SiPM is a so called avalanche photodiode, operated in reversed bias mode. The typical doping scheme of these diodes is a combination of intrinsic and doped semiconductors (p^+i-p-n^+). Photons hitting the intrinsic region of the pixel creating electron-hole pairs. Due to the reversed bias applied the electrons drift to the multiplication region created by the $p-n^+$ -junction. Further electron-hole pairs are created due to the acceleration of the charges in the high electric field. Choosing a bias voltage lower than the breakdown voltage, the diode operates in the so called linear mode where the drawn current is proportional to the incident number of photons. By operating above breakdown, in the so called Geiger mode, the initial electron-hole pair creates an avalanche of further charge carriers.

A quenching resistor in series drops the voltage and stops the avalanche. In the avalanche mode the collected charge per pixel does not depend on the number of the primary charge carriers and thus of the number of incident photons in this pixel. But since each channel of the SiPM comprises multiple pixels, multiple photons hitting the same channel can be counted by summing the output of the pixels.

3.6.3 Characterization

The SiPMs are characterized by several parameters which can differ between different versions of the used SiPMs. The most important ones are described below.

Breakdown Voltage. The breakdown voltage is defined as the voltage at which the electric field of the multiplication area becomes large enough to create an avalanche of electron-hole pairs. The so called overvoltage (U_{OV}) is defined as the difference between the applied bias voltage and the specific breakdown voltage:

$$U_{OV} = U_{BIAS} - U_{BD}$$

The resulting electric field inside the SiPM is proportional to the applied overvoltage.

Gain. The gain of the detector is defined as the multiplication factor of an elementary charge e in the avalanche and is a function of the overvoltage and the capacity of the pixel:

$$G = \frac{Q_{avalanche}}{e} = \frac{U_{OV} \cdot C}{e}$$

with $Q_{avalanche}$ the charge of a single avalanche. Due to the linear dependence on the over-voltage and the capacity C of each pixel, each avalanche creates a similar signal. The gain can be determined by measuring the charge difference between a signal with n pixels firing and a signal with $n + 1$ pixels firing, where n is a small integer value. The left side of Figure 4.4 in Chapter 4 shows the resulting charge spectrum. The distance between two peaks corresponds to the charge of a single avalanche.

Photon Detection Efficiency (PDE). The PDE is defined as the ratio between the number of detected photons and the total number of incident photons:

$$PDE = \frac{N_{detected}}{N_{total}} = QE \cdot \epsilon_{Geiger}(T, V) \cdot \epsilon_G$$

It depends linearly on the quantum efficiency (QE), the Geiger efficiency ϵ_{Geiger} and the geometric fill factor ϵ_G . The quantum efficiency describes the probability that an incident photon creates an electron-hole pair. The Geiger efficiency, which depends on the temperature and the applied voltage, describes the probability that the electron-hole pair induces an avalanche. The geometric fill factor accounts for the insensitive part of each pixel. The PDE of the SiPM versions used is in the order of 40-50%.

Dark Count Rate (DCR). The dark count rate is defined as the rate at which pixels fire with no incident light due to thermally produced charge carriers in the conduction band. Neutron irradiation will damage the crystal structure and will lead to interstitial atoms with any energy level close to the conduction band. This leads to an increased probability of thermally produced charge carriers in the conduction band. SiPMs which have seen a large neutron fluence show an increased DCR. Since this noise depends on the temperature it can be reduced by cooling the detectors. The first peak (pedestal peak) of the ADC spectrum (see Figure 4.4 in Chapter 4) is dominantly produced by the DCR and the noise from the electronics.

Cross-talk (x-talk). Every electron in an avalanche of the SiPM is accelerated and therefore has the probability to emit synchrotron photons. Due to these infrared photons, neighbouring pixels can be triggered which lead to cross-talk. The amplitude of the cross-talk signal is generally one photoelectron and the probability is proportional to the gain.

After-pulses. Impurities in the crystal structure of the silicon, like damage to the lattice structure or an unwanted nuclei, create energy levels in the band gap. Electrons and holes trapped in these impurity levels can produce delayed avalanches with a variable amplitude. These cannot be distinguished from the signal.

3.7 Clusterization

In order to be able to read out more than 500,000 channels in total, at a rate of 40 MHz, it is necessary to reduce the amount of data directly in the front-end electronics. A cluster-algorithm is performed to suppress noise and reduce the amount of data significantly.

Particles passing through the fibre mat will create a signal not only in one SiPM channel, but in the neighbouring ones as well. By finding clusters of neighbouring channels, whose signals exceed certain thresholds, the amplitude and the barycentre of the cluster is calculated. Therefore three thresholds are defined: *low*, *middle* and *high*. The algorithm starts by finding a channel which signal passes the *middle* threshold. The cluster is filled up with neighbouring channels, as long as their signal exceed the *low* threshold. In order to pass the cluster-algorithm, the sum of the signals in the channels of the cluster has to exceed the *high* threshold.

The signal in every channel can now be represented in terms of 3 bits (*low* 001, *middle* 011, *high* 111). But since there are only four possible outcomes when assuming $low < middle < high$, the signal can be transferred by using only two bits (00,01,10,11). A cluster require the 2-bit sum of neighbouring channels to be greater or equal to 3 in decimal value to pass the cluster algorithm.

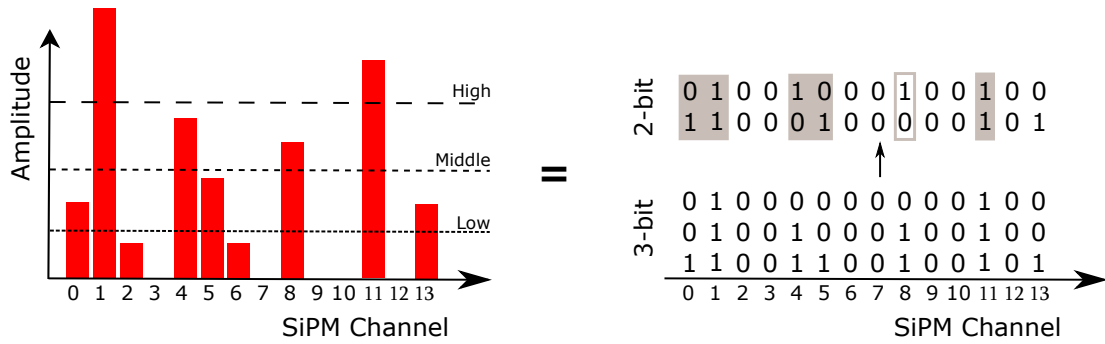


Figure 3.14: Illustration of the clustering algorithm and the 3- and 2-bit representation of the cluster thresholds. The grey boxes illustrate found clusters while the open grey box fails the cluster algorithm due to failing the sum threshold. [24]

3.8 Readout Electronics

The functional architecture of the front-end read-out electronics is shown in Figure 3.15. The signal coming from the SiPMs is amplified, shaped and digitized in a specially developed integrated circuit (ASIC), called PACIFIC (a low Power ASIC for the sCIntillating FIBres traCker). Afterwards the digitized signal is routed to the cluster-board with an FPGA (field programmable gate array) which executes the clustering algorithm and zero suppression to reduce the data volume. The data from all the SiPMs of one fibre mat is then combined by an FPGA in the master-board and transferred via optical links to the back-end side of the DAQ system.

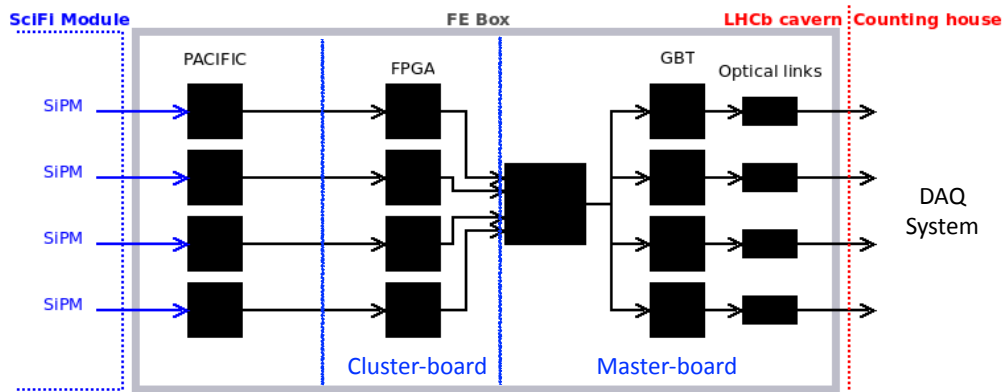


Figure 3.15: Functional diagram of the front-end electronics. [4] (modified)

4 Test Stand for Fibre Mat Qualification

During the course of this thesis a setup to measure the light yield of ionizing particles produced in fibre mats was build up, which is described in this chapter.

4.1 Motivation

In order to have high hit efficiency and a good spatial resolution for ionizing particles in the detector, it is necessary that the light produced in the scintillating fibres and detected by the SiPMs is sufficient. Therefore our most important measured parameter is the light yield in units of photoelectrons. There are several effects which can reduce the light yield for an ionizing particle on the way to the SiPM detectors. Always present is the attenuation of the scintillation light which reduces the yield depending on the travelled distance in the fibres. Due to the highly non-uniform irradiation during operation of the LHC, the fibres will experience a different dose depending on the position in the detector. The irradiation will lead to a darkening of the fibres which reduces the amount of light arriving at the SiPMs. This effect is described in more detail in Chapter 5. Additional to these effects, damages due to the handling during the serial production can occur. This includes, for example, cracks inside the fibre matrix, damages on the mirror and damages on the edges of the fibre mats due to the longitudinal cut. These effects are described in more detail in Chapter 6. An experimental setup was developed to measure the light yield of ionizing particles passing through the fibre mats and modules.

4.2 Test Stand for Light Yield Measurements

Figure 5.12 shows a schematic of the test stand used for light yield measurements of single fibre mats. The light produced in the fibres is detected by four arrays of SiPM which are connected to a front-end board. The front-end board, containing a pre-amplifier ASIC (Application Specific Integrated Circuit), called SPIROC-A, is read out by the so called USBBoard data acquisition system (DAQ). The software "strosmic90"¹ is used to read out the USBBoard DAQ. In order to read out only events where ionizing particles passing through the fibre mat, a trigger system is build up.

Two different versions of SiPM produced by Hamamatsu² are used with slightly

¹Software developed by Roman Greim, RWTH Aachen, <https://gitlab.cern.ch/lhcb-scifi/sci-fusbboard/tree/master/utils/strosmic90>

²Hamamatsu Photonics K.K., 325-6, Sunayama-cho, Naka-ku, Hamamatsu City, Shizuoka Pref., 430-8587, Japan.

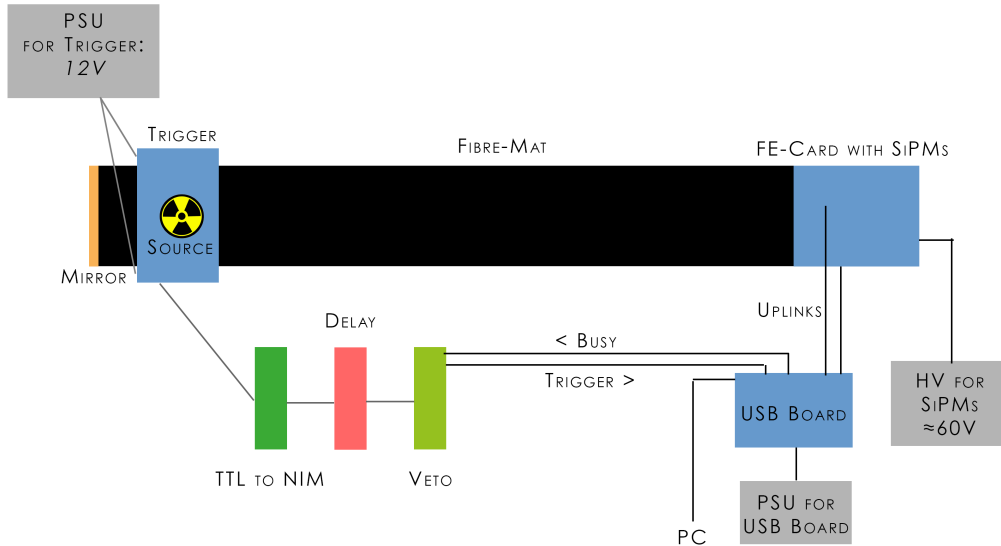


Figure 4.1: Schematic of the ^{90}Sr test stand.

different specifications as shown in Table 4.1 [25]. The detectors are operated at $\Delta V = 3.5 \text{ V}$ overvoltage.

For measurements of full size fibre modules, the test stand is extended such that in total 32 arrays of SiPMs are read out simultaneously. Therefore two USB-Board DAQs read out eight front-end boards each. The following sections give a more detailed description of the components of the test stands.

Table 4.1: Comparison of H2014 and H2015 Hamamatsu SiPM version at 3.5 V over-voltage [25].

Version	Channel size [μm]	direct x-talk	delayed x-talk	After-pulse	PDE
H2014	230×1500	17%	5.5%	1.8%	39%
H2015	230×1625	4.5%	1.8%	6.5%	47%

4.2.1 Readout Electronics

SPIROC-A The EASIROC chip, which was originally designed for the Analogue Hadronic Calorimeter at the International Linear Collider, also known as the SPIROC-A (Silicon PM Integrates Read Out Chip - Analogue), is a 32 channel pre-amplifier ASIC [26]. It consist of a pre-amplifier, shaper and a track-and-hold block for each channel. The shaper has a shaping time of approximately 200 ns. An analogue buffer stores the sampled result for each channel which get multiplexed for output channel by channel by an external control signal. To compensate possible variations of the intrinsic breakdown voltage of the SiPMs in each channel, an 8-bit DAC is attached which allows the fine-tuning of the overvoltage [27].

USB-Board DAQ Specifically designed for multi-channel SiPM read-out, the USB-Board data acquisition system is a general purpose DAQ which can read out different ASICs with similar structure as described above. The DAQ is used to digitize and read-out the front-end boards and it also provides a slow control interface as well as the read out of on-board sensors like temperature and current. The USBBoard-DAQ is able to read out up to eight front-end boards simultaneously.

Figure 4.2 shows the main functional blocks of the USB-Board DAQ. The analogue signals coming from the front-end boards via uplink cables are first multiplexed in the USBBoard, then digitized by 12-bit ADCs and stored in the FPGA's FIFO (first in first out) buffer until it is read out via a USB interface by a PC. Two laser mezzanine sockets, providing four channels of fast-rising light pulses, are used for the light injection system to calibrate the SiPMs. The slow control interface, used to control the 8-bit DAC for the fine-tuning of the overvoltage on the SPIROC chips is implemented in the FPGA.

Since the USB-Board is an asynchronous system, it needs a trigger signal to readout the event. Each triggered event will sample the multiplexed analogue output channel by channel which gets combined and saved in the FIFO. The USB-Board provides two trigger modes, the self-trigger mode used for pedestal and light calibration data taking and the external trigger mode used for data taking of ionizing particles. The self-trigger mode generates a configurable periodic signal. The external trigger mode needs an external negative NIM level signal which should be between 50 and 200 ns to assure correctly registered trigger events. Additionally the external trigger has to be vetoed with the BUSY signal to avoid data taking while the FIFO is full and ready to read-out [27].

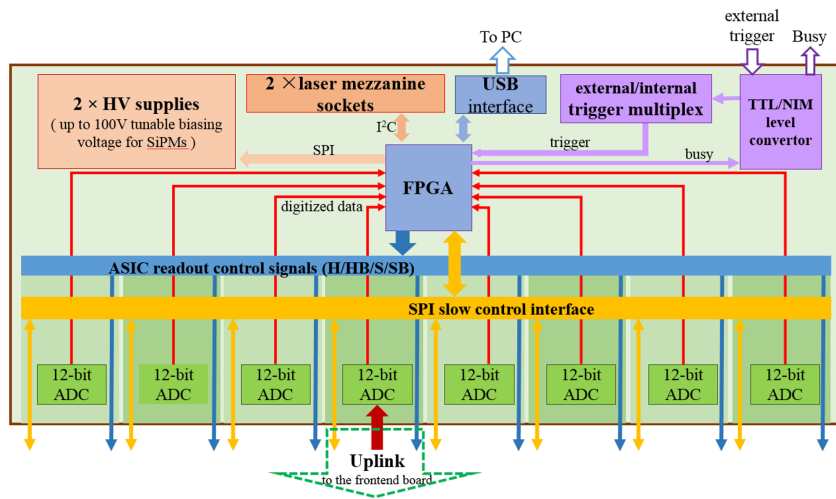


Figure 4.2: Main functional blocks and signal flow of the USB-Board data acquisition system. [27]

4.2.2 Particle Trigger System

The external trigger used in the experimental setup is generated by a scintillator. Two single channel SiPMs from Hamamatsu (model S13360-3050CS), $3 \times 3 \text{ mm}^2$ in size, are used to detect the scintillation light. The trigger for the single fibre mat test stand uses a scintillating bar with the dimension $1 \times 1 \times 17 \text{ cm}^3$. The trigger for the full module test stand uses a larger scintillating plastic paddle with the dimension $1.5 \times 18 \times 57.5 \text{ cm}^3$. To capture the photons generated in the scintillator paddle and to guide it to the SiPMs, two wavelength shifting fibres are glued inside the paddle which are connected to one of the described SiPM each. Figure 4.3 shows the two different triggers used. In order to trigger only on minimum ionizing particles, one millimeter of plastic is introduced between the fibre mat and the scintillating bar of the trigger, stopping the low energy electrons.

The electronics to process the signals from the SiPMs include an amplifier with adjustable gain and a discriminator. To reduce the amount of fake trigger, a coincidence of both SiPM signals is formed. The output of the trigger is converted from TTL to NIM standard signal to match the input of the USB-Board trigger input. To make sure the timing of the trigger signal matches the read-out of the USB-Board, a delay unit is used to adjust the timing. A logic unit vetoes the trigger signal with the BUSY output of the USB-Board.

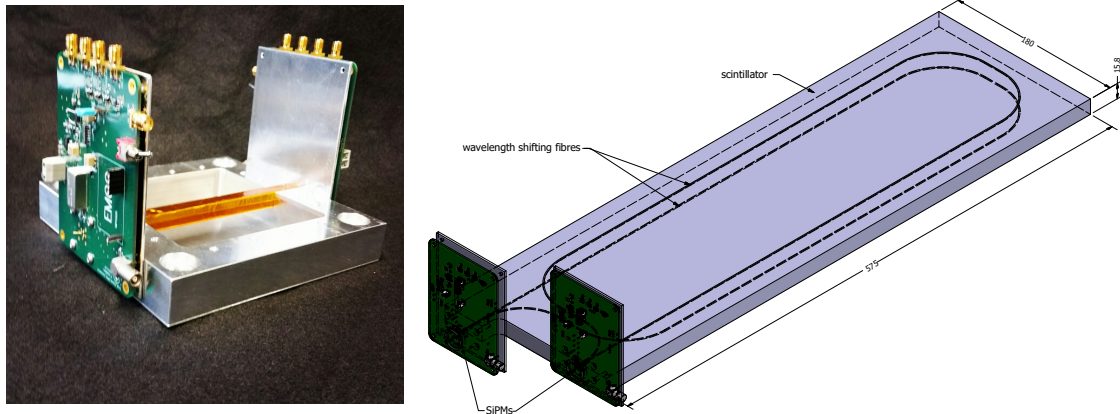


Figure 4.3: *Left:* Scintillating bar trigger used for single fibre mat measurements. The scintillating bar is equipped with one single channel SiPM on each side with dedicated electronics. *Right:* Scintillating pad trigger used for full size module measurements. Each wavelength shifting fibre is connected to a single channel SiPM separately. [28]

4.2.3 SiPM Calibration for Fibre Mat Read-Out

In order to ensure a uniform detector response over all SiPM channels, the arrays have to be calibrated concerning their overvoltage. Since all channels have a slightly different intrinsic breakdown voltage, operating them at the same bias voltage would lead to different over-voltages in each channel, which in turn leads to a slightly different PDE. Therefore each channel has its own DAC to fine-tune the overvoltage which can be set via the slow control interface of the USB-Board.

To measure and compare the intrinsic breakdown voltage of each channel, light has to be injected homogeneously. This is done using the laser mezzanines of the USB-Board combined with the light injection bars produced for the module assembly. The trigger of the USB-Board is therefore switched to self-trigger mode.

The intrinsic breakdown voltage of every channel can be determined by measuring the gain in each channel at different bias voltages. On the left side of Figure 4.4 the ADC spectrum for a single channel is plotted. The visible peaks correspond to the number of detected photons while the first peak is the pedestal generated by noise. To determine the gain, the peaks are fitted with a gaussian to determine the position of their maximum. The difference in ADC values between each peak is then calculated and in case they differ, the distances of the peaks are averaged. This is done for every channel for at least 6 different bias voltages in order to minimize the uncertainty of a linear fit performed afterwards. The right side of Figure 4.4 shows the correlation between the gain and the applied voltage for one single channel. The points are fitted with a linear function to determine the voltage where the gain vanishes, which corresponds to the intrinsic breakdown voltage.

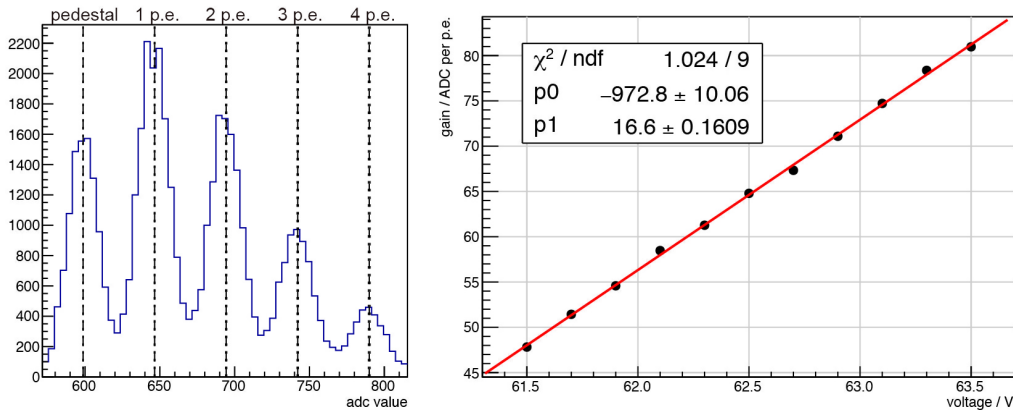


Figure 4.4: *Left:* ADC spectrum of a single channel using the light injection system. The photo peaks are fitted to determine the gain. *Right:* Gain vs applied voltage for one channel. The extrapolation to the x-intercept lead to the intrinsic breakdown voltage of this channel.

To compensate variations of the intrinsic breakdown voltage, each channel has an 8-bit DAC which allows the fine-tuning of the overvoltage within 4.2 V. With 8

bits, the voltage range of 4.2 V can be divided in 256 steps of 16 mV. To minimize these variations, a breakdown voltage ($U_{\text{bd}}^{\text{desired}}$) is chosen at which the SiPMs should operate. The difference between the measured intrinsic breakdown voltage ($U_{\text{bd}}^{\text{intrinsic}}$) and the desired breakdown voltage is calculated and converted into an DAC value. The new DAC value, to fine-tune each channel, can be calculated with:

$$\text{DAC}_{\text{new}} = \frac{U_{\text{bd}}^{\text{intrinsic}} - U_{\text{bd}}^{\text{desired}}}{0.016} + \text{DAC}_{\text{old}}$$

where DAC_{old} is the DAC value which was set before.

The distribution of the breakdown voltage for all 512 channels is plotted in Figure 4.5. The spread of the distribution (RMS) before the calibration is 81.4 mV. After four calibration runs the spread was reduced to 72.7 mV at a breakdown voltage of $U_{\text{bd}}^{\text{desired}} = 58.6$ V. Since the four SiPM arrays were already preselected with respect to their mean intrinsic breakdown voltage, the spread of the distribution before the calibration was already rather small. Depending on the SiPM arrays used, the initial spread of the intrinsic breakdown voltage distribution can be up to several 100 mV. By operating the SiPMs at 3.5 V overvoltage, the corresponding bias voltage is $U_{\text{BIAS}} = U_{\text{bd}}^{\text{desired}} + 3.5$ V = 62.1 V.

The same routine is also used for the calibration of the full size module with 32 arrays of SiPMs and a total of 2048 channels.

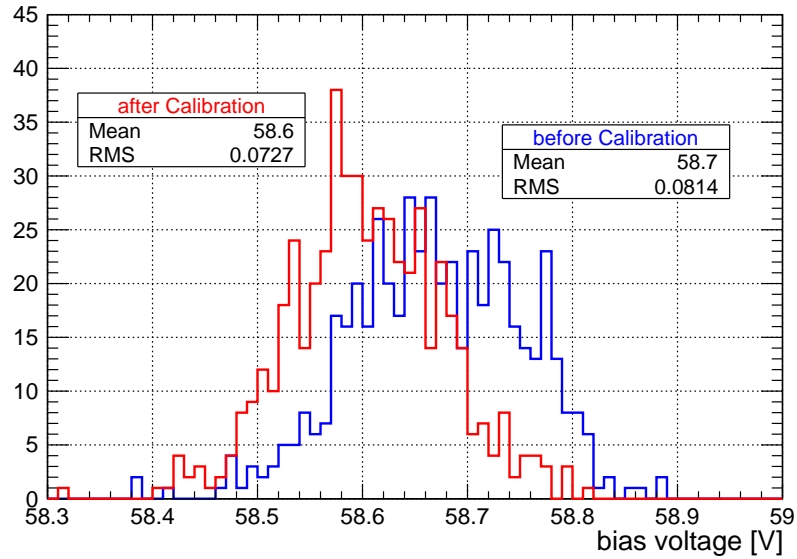
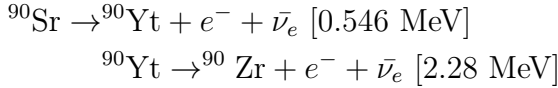


Figure 4.5: Distribution of the breakdown voltages of all 512 channels before (*blue*) and after (*red*) calibration. Due to the calibration the spread of the distribution is reduced from 81.4 mV to 72.7 mV.

4.2.4 Particle Sources

Several different sources of ionizing particles are used to characterize the fibre mats and modules. A ^{90}Sr beta source was used mainly for the single fibre mat light yield measurements. Due to the dimensions of a full module, muons from cosmic rays rather than a beta source were used for the full module measurements. A study of using cosmic rays for quality assurance measurements can be found in reference [29]. Particle beams from the SPS at CERN were used to study the light yield and the single hit efficiency of an irradiated test module.

Beta electrons. For the quality assurance measurements of the fibre mats a 3.7 MBq Strontium-90 source is used. ^{90}Sr is a radioactive isotope with a half-life of 28.8 years and a decay energy of 0.546 MeV. It undergoes beta decay to Yttrium-90 which itself decays to the stable Zirconium-90 under the emission of an electron and anti-neutrino and a decay energy of 2.28 MeV:



The $^{90}\text{Sr90}$ source used for the fibre mat measurements is positioned 11cm above the centre of the fibre mat, close (13 cm) to the mirror. Due to the large aperture of the source, the fibre mat gets rather homogeneously irradiated over the full width. The source used during measurements at CERN has a small aperture, so it had to be moved to 3 positions to irradiate the full width of the fibre mat with sufficient particles.

Cosmic muons. Primary cosmic rays, which consist of a mixture of protons with some α -particles, are striking the earth's atmosphere with very high energies up to 10^{12} GeV. These cosmic rays are hitting the molecules in the upper atmosphere, mainly nitrogen and oxygen, and induce a cascade of weak decays of neutrons, pions and muons forming the so called secondary cosmic rays [30]. Figure 4.6 illustrates this process. The muons are generated at about 10 km height and reach the earth surface due to their relativistic energies. The rate of incident cosmic muon at sea level is approximately 100 particles/($\text{m}^2 \cdot \text{s} \cdot \text{sterad}$) [31].

Test beam. At CERN's North Area SPS Test Beam Facility protons from the SPS with an energy of 450 GeV are shot on a target creating a secondary beam. This secondary beam consists mainly of protons ($\approx 60\%$), pions ($\approx 20\%$) and muons ($\approx 10\%$) with a momentum of 180 GeV/c. By closing a shutter the protons and pions get nearly completely blocked which leads to a clean muon beam. The mixed pion beam as well as the muon beam were used to study the light yield and hit efficiency on an irradiated SciFi test module.

SiPM channels. Therefore each event is going through a clustering algorithm. This means to search for patterns in the whole channel range of each event which get combined to one cluster. The applied cluster algorithm is similar to the one which will be used in the PACIFIC read-out in the LHCb upgrade detector.

The algorithm searches for channels which exceed the so-called *seed* threshold. If it has found one it adds the channels to the right and to the left as long as they exceed the lower *neighbour* threshold. Finally the sum of the charge of all channels of the cluster candidate has to pass the *sum* threshold. If one cluster candidate passes this algorithm the total charge of the cluster is assigned to the channel which corresponds to the channel of the mean position. If not stated different, the common thresholds in units of photoelectrons (p.e.) used in this thesis are:

- seed threshold: **2.5 p.e.**
- neighbour threshold: **1.5 p.e.**
- sum threshold: **2.5 p.e.**

Using a ^{90}Sr source, positioned at the mirror end of the fibre mat, this leads to a distribution of the cluster charges in units of photoelectrons in each channel as shown in Figure 4.7, with a mean value of around 20 p.e..

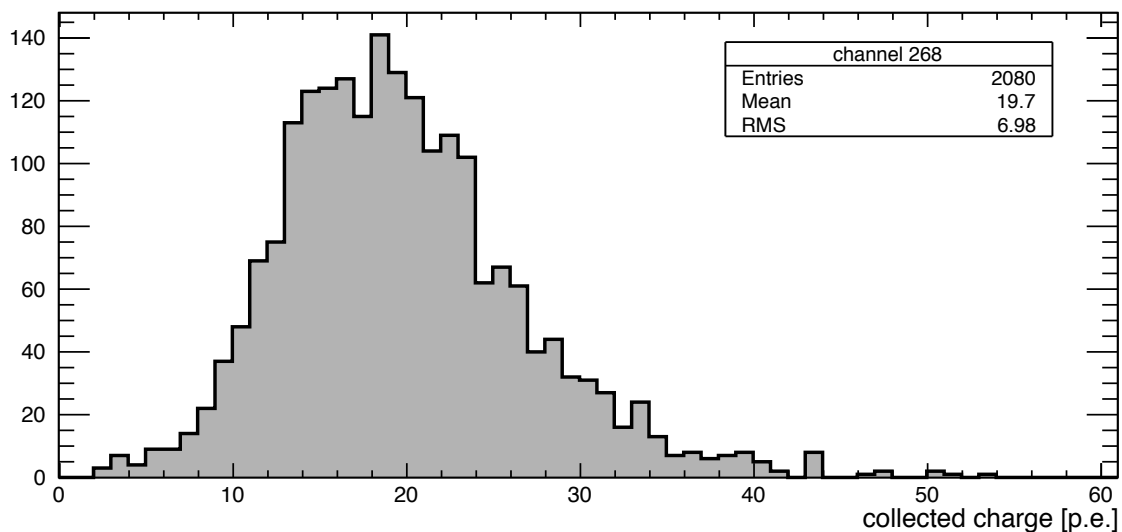


Figure 4.7: Distribution of the collected cluster charges in units of photoelectrons in channel 268.

The mean value of the distribution of the collected charge is called light yield. Figure 4.8 shows the light yield in every channel for a single fibre mat measured with the ^{90}Sr source near the mirror.

The light yield of this particular fibre mat is very homogeneous over the full width of the fibre mat with no visible defects. A drop in light yield occurs every 64

channels due to the gaps between the SiPM dies as well as the gaps between the SiPM arrays. Since the gaps are corresponding to one channel width, the missing charge in the clusters around the gaps results in a reduced light yield of about 30% in the neighbouring channels. The additional gap around channel 364 is caused by a broken SiPM channel. Due to the same clustering effect the light yield of the neighbouring channels is similarly reduced.

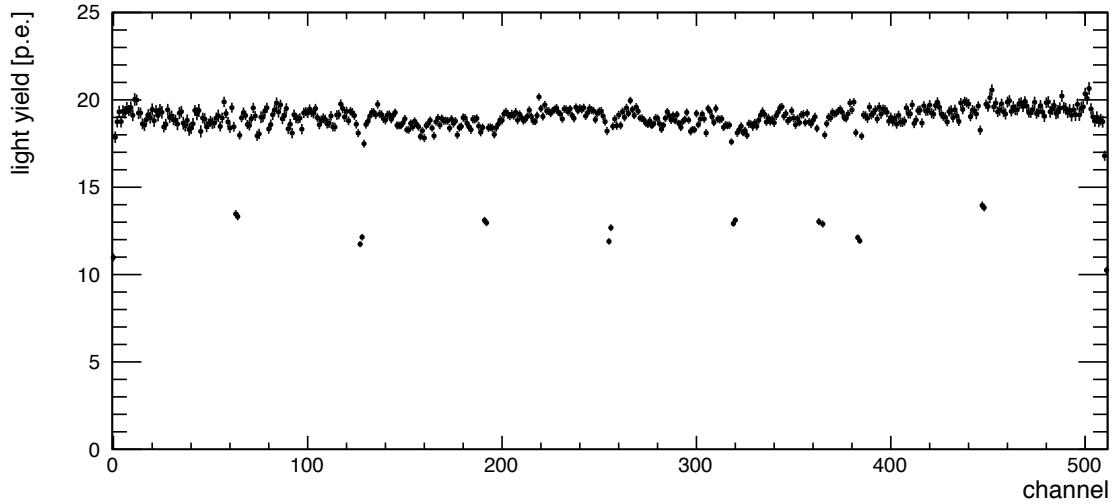


Figure 4.8: Mean light yield of a single fibre mat measured near the mirror. The light yield is very homogeneous over the full width of the fibre mat. The structures every 64 channels are due to the gaps between the SiPM arrays as well as the SiPM dies. The additional gap around channel 364 is due to a broken SiPM channel.

The edges of the fibre mats might show also a drop in light yield due to two reasons. The first is obviously again the missing charge of the neighbouring channel of the cluster. The second is due to a damage of the fibres during the longitudinal cut. This is described in more detail in Chapter 6.

5 Scintillating Fibre Radiation Damage

This chapter studies the radiation damage of scintillating fibres by ionizing radiation as well as the consequences in terms of expected detector performance. Test modules have been irradiated to the expected lifetime dose profile, surveyed afterwards and characterized in a particle beam.

5.1 Introduction

To guarantee a high efficiency of the SciFi Tracker for charged particles, it is essential to ensure enough light reaching the SiPMs over the full lifetime of the detector. Due to the highly non-uniform radiation environment at the LHCb, the scintillating fibres will suffer from radiation effects, especially around the beampipe.

The irradiation of scintillating fibres by ionizing particles can destroy the fluorescent dyes of the scintillator and shortens the attenuation length of the fibre due to an increase in the number of scattering centres in the plastic. This depends on the material of the scintillating fibre as well as the radiation dose [16].

In the scintillating fibres used for the SciFi Tracker, the destruction of the fluorescent dyes can be neglected [32]. Early investigations of the radiation damage on plastic scintillating fibres showed that the main cause for degradation in light output is due to optical changes of the base material [33]. The most relevant irradiation effect is the formation of absorption and scattering centres which increase the attenuation of the light transmission inside the fibre due to the creation of free radicals [19]. Free radicals are ions with unpaired valence electrons, which are highly reactive and absorb light strongly in the blue and UV regions. Free radicals annihilate when two come together by exchanging their valence electrons. The creation of radicals during irradiation is proportional to the radiation dose while the decay rate is proportional to the square of the concentration of radicals. Observations of the light transmission during irradiation showed that the transmission decreases until a saturation of free radicals is reached.

Three different types of absorption centres were found, which effect the attenuation [19]. One type causes a permanent damage, which is depending linearly on the dose with only a small contribution. The second type of absorption centres are radicals which, in the presence of oxygen, annihilate leading to an annealing of the fibre. If the existing oxygen is consumed the contribution is also permanent since they won't annihilate anymore. Depending on the dose rate of the irradiation, the speed of the annealing process is influenced. During high dose-rate irradiations the oxygen is consumed faster than it can diffuse into the fibre, while at low dose-rates the oxygen is available during the irradiation. The third type, the short-lived absorption centres

decay whether oxygen is present or not with different decay times [19]. Since the effect of the irradiation on the six layer fibre modules has not been well tested yet, this thesis focusses on the damage due to the irradiation and the performance afterwards.

5.2 Module Irradiation at CERN

To study the effect of the expected irradiation foreseen for the detector after the upgrade, test modules have been irradiated with the expected dose profile. These modules have been characterized as a function of time, beginning directly after the irradiation. The single hit efficiency has been determined with a particle beam.

5.2.1 Module Design

The test module is build out of one single 6-layer fibre mat. It is sandwiched between two half-panels made out of 19.7 mm high Nomex honey-comb cores laminated on one side with a 200 g m^{-2} carbon-fibre reinforced polymer skin. For the bonding between fibre mat and honey-comb an Araldite epoxy is used. At the readout side of the module aluminium blocks have been added for mechanical fixation and mounting of enclosures and electronics. The other side is equipped with a mylar mirror foil of $60 \mu\text{m}$ thickness which is vacuum coated at CERN with an Al/MgF₂ pair (90 nm/20 nm thickness) coating [24].

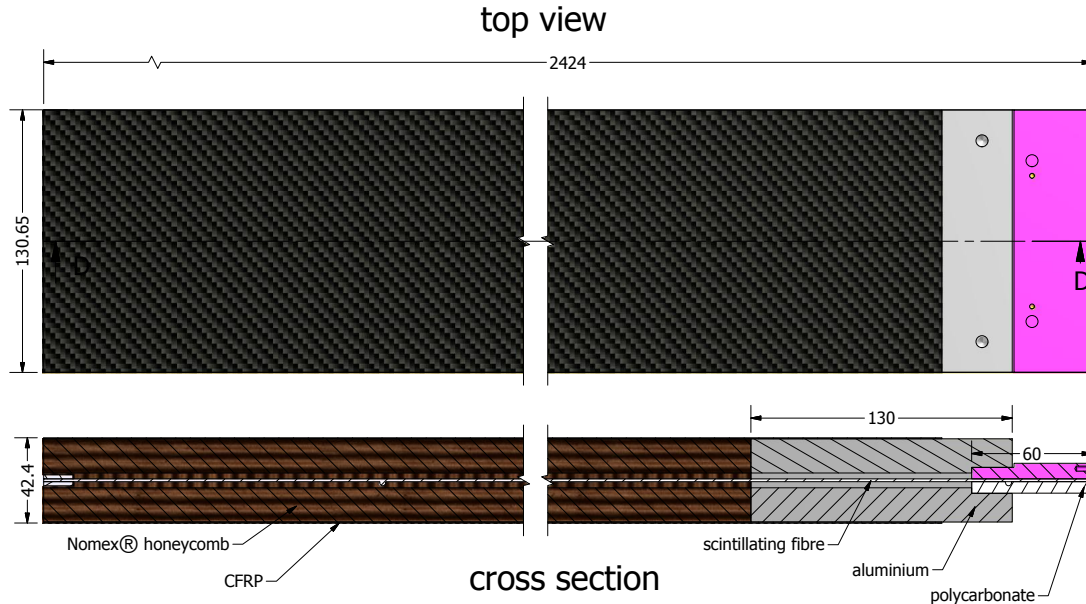


Figure 5.1: Illustration of the single fibre mat test module design. [24]

5.2.2 Irradiation Parameters

Corresponding to the expected integrated luminosity of 50 fb^{-1} up to which the SciFi detector will operate, the expected irradiation dose ranges from up to 40 kGy in the region close to the mirror down to around 100 Gy in the readout region of the modules [34].

In October 2015 and in July 2016 two test modules have been irradiated at the CERN IRRAD PS facility with 24 GeV protons. The modules were positioned such that the beam centre will hit the module 40 mm from the edge. The deposited irradiation dose was measured with aluminium strips which were fixed on the module. During irradiation aluminium is activated to ^{24}Na and ^{22}Na . By evaluating the ^{22}Na activity after irradiation with a germanium detector, the number of protons which hit the aluminium can be determined, from which the dose can be calculated. Figure 5.2 shows the expected dose as well as the dose measured by the ^{22}Na dosimetry.

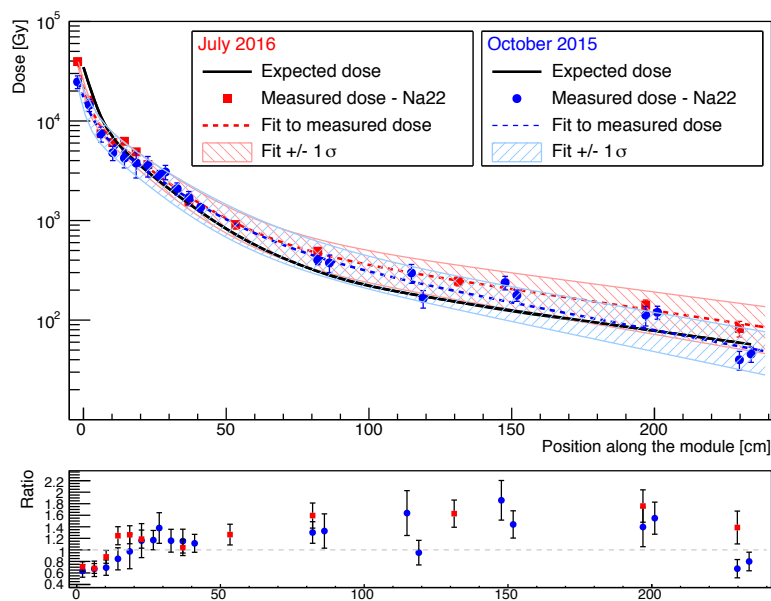


Figure 5.2: Measured and expected irradiation dose of both test modules irradiated at IRRAD PS as function of the module position. Position 0cm (left side) corresponds to the mirror side. The black line indicates the expected dose whereas the red (July 2016), respectively blue (October 2015) points show the ^{22}Na measurements of the dose. The shaded areas are showing the $\pm 1\sigma$ envelope. The plot on the bottom shows additionally the ratio of measured and targeted dose. [35]

5.2.3 Previous Light Yield Measurements

The light yield of a module irradiated in October 2015, has been measured in a particle beam in November 2015, a couple of days after the irradiation. Figure 5.3 shows the light yield in the non-irradiated and the irradiated region measured in the particle beam (*green*) compared to an ^{90}Sr measurement (*blue*), which was done several months later in Heidelberg. The measurement done with the particle beam resulted in a light yield of around 13 p.e. in the non-irradiated and 5 p.e. in the irradiated region. Whereas the ^{90}Sr measurement showed a light yield of around 14 p.e. in the non-irradiated and 9 p.e. in the irradiated region respectively. Up to around 10% difference between both measurement runs might be due to the different energy spectra of the minimum ionizing particles in the beam and the ^{90}Sr source, as seen in the non-irradiated region. But the difference in the irradiated region is much higher, around 45%. To investigate whether this difference is a time dependent effect, light yield measurements of the module irradiated in July 2016 have been done on a daily basis, starting directly after the irradiation.

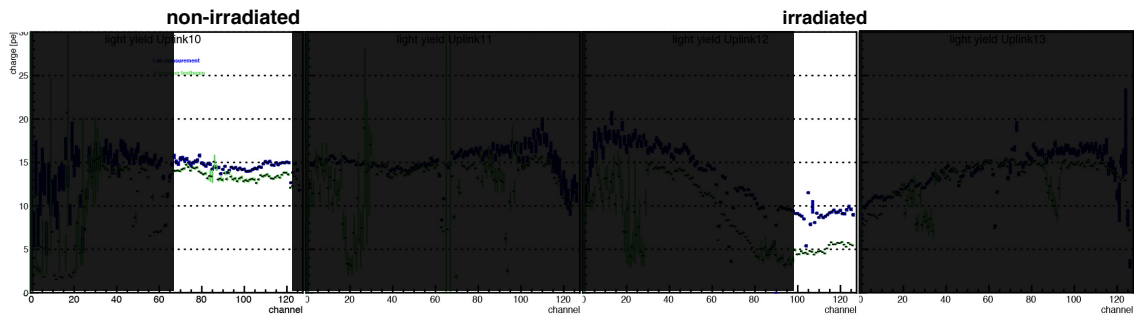


Figure 5.3: Comparison of the measurement from the last beam test in November 2015 (*green*) and a measurement taken several months later in Heidelberg (*blue*) with a ^{90}Sr source. The plot is showing the light yield for each channel in the non-irradiated (*left*) and irradiated (*right*) region. [24] (modified)

5.3 Time Dependence of the Irradiation Effect

To investigate the time behaviour of the radiation damage on the 2016 irradiated test module, the light yield measurements have been performed before and after the irradiation using a ^{90}Sr source. Measurements after the irradiation have been made on a daily basis to observe the module over time.

5.3.1 Initial Characterization

To characterize the module before the irradiation, light yield measurements have been performed in Heidelberg. The source was placed 11 cm above the centre of the

module. Several points along the mat were measured as shown in Figure 5.4. Since the gradient of the expected irradiation dose is much stronger near the mirror the initial measurements are also denser there.



Figure 5.4: Illustration of the measured positions (blue lines) along the fibre mat in Heidelberg.

The mean light yield measured before the irradiation near the mirror is shown in Figure 5.5. There are a couple of features visible which are related to the readout electronics and not the fibre mat itself. First the dips in light yield every 64 channels are due to the gaps between the SiPM dies. These gaps have the width of one SiPM channel. Additionally there are two damaged channels (channel 95, 384) which do not see any light. Therefore the neighbouring channel see a lower light yield since the cluster algorithm is missing the light of these damaged channels. The third feature is a slight decrease in light yield from channel 384 to the right edge of the mat which is due to a light leak on the right edge. Ambient light is entering the fibre mat and induce additional low amplitude clusters, which reduce the mean light yield. Besides these features, the average light yield for the channels is homogeneous at around 16 p.e.

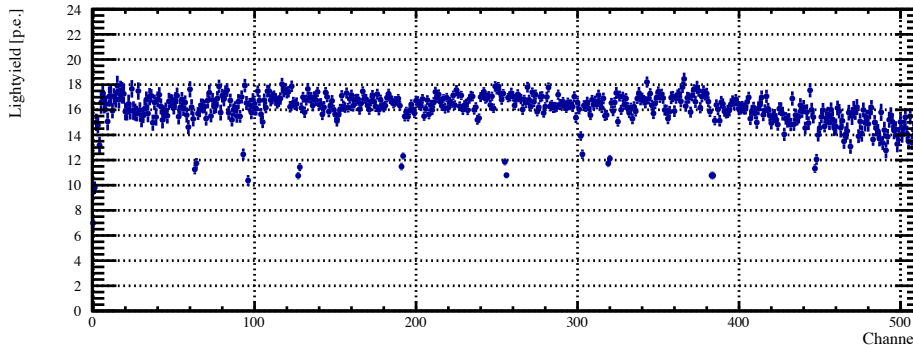


Figure 5.5: Measurement of the light yield 2 cm in front of the mirror before irradiation. The slope on the right side is due to a small light leak on the edge which induces low amplitude clusters.

In order to get the light yield as a function of longitudinal position in the fibre mats, the light yield for channel 130 to 380 (excluding the SiPM gaps) are averaged for the different longitudinal positions and plotted as a function of the distance from the SiPM. As shown in Figure 5.6, the light yield increases towards the read-out side from 16 p.e. to around 23 p.e. at 20 cm in front of the SiPMs.

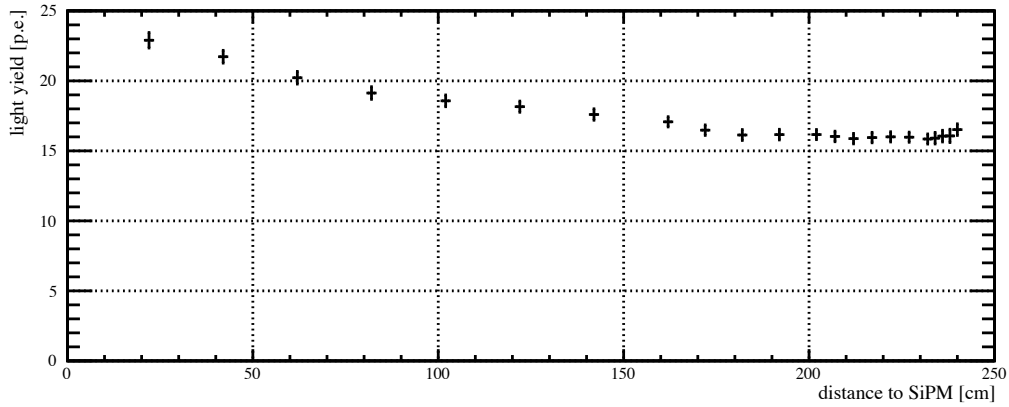


Figure 5.6: Measurement of the light yield along the mat length obtained by averaging the light yield for channels 130 to 380 for the different longitudinal positions.

5.3.2 Characterization After Irradiation

The ^{90}Sr source used at CERN differs slightly from the one used in the measurements before the irradiation in Heidelberg. It has a rather small aperture, so one had to move the source to three positions in order to cover most of the width of the fibre mat. Since this is more time consuming not all points which have been measured in Heidelberg were measured at CERN. These full module scan measurements were made one day, six days, 16 days and 35 days after the irradiation. Additionally the positions at 2 cm and at 30 cm in front of the mirror were measured on a daily basis.

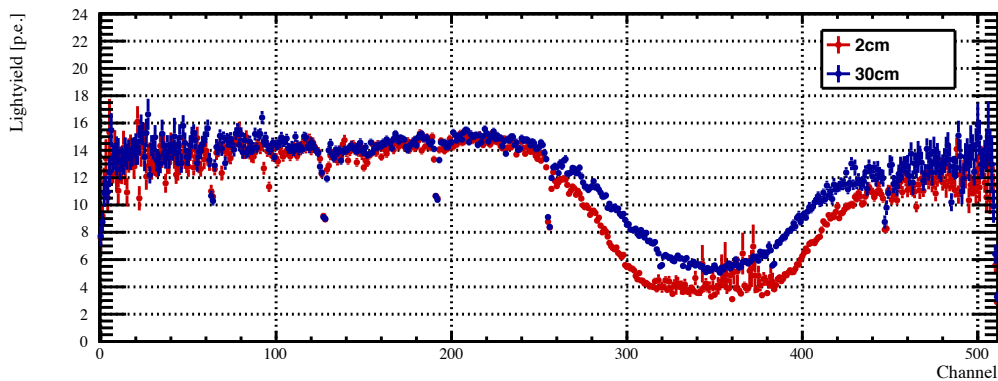


Figure 5.7: Light yield measurement of the irradiated module one day after the irradiation at two longitudinal positions. One clearly sees the drop in light yield in the irradiated region between channel 240 and 440.

Figure 5.7 shows the light yield measurements of two longitudinal positions done one day after the irradiation. The light yield in the irradiated region drops between channels 240 and 440 to around 4 p.e. for the position near the mirror and to around

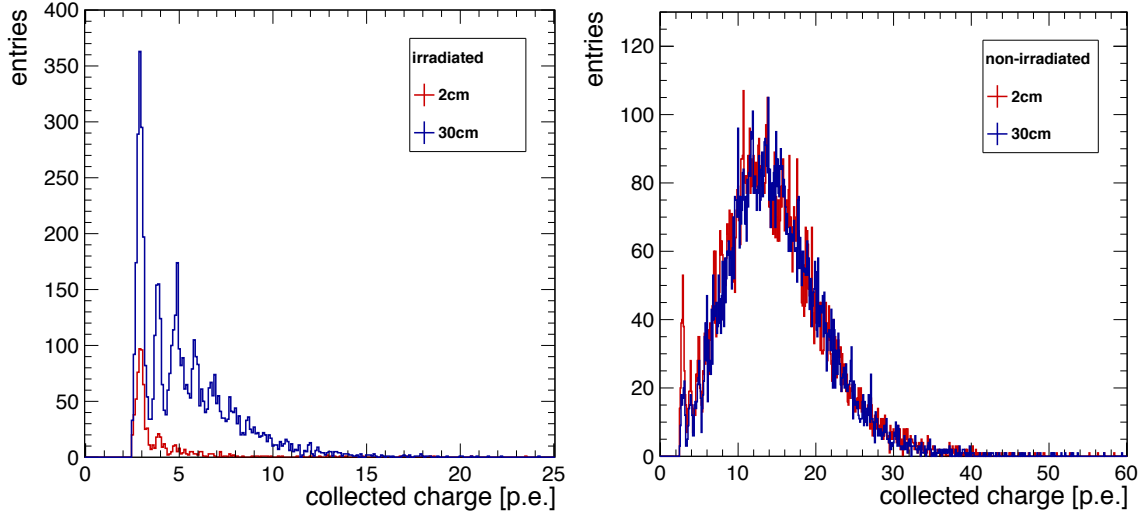


Figure 5.8: Charge distribution in the irradiated (*left*) and non-irradiated (*right*) region for the 2 cm and the 30 cm measurements.

5.5 p.e. at the position 30 cm in front of the mirror. It turned out that the light yield measured in the irradiated region is biased toward higher values because the cluster algorithm exclude events with cluster charges lower than 2.5 p.e.. By lowering the thresholds of the cluster algorithm to 1.5 p.e. for seed, 0.5 p.e. for neighbour and 1.5 p.e. for the sum, the light yield in the irradiated region near the mirror drops to around 2.5 p.e.. With this low light yield it is not possible anymore to have a efficient separation of the signal and the pedestal generated by noise.

The light yield in the non-irradiated region on the left side of the fibre mat is for both longitudinal positions nearly the same at around 14-15 p.e.. However the yield in the non-irradiated region on the right edge of the mat is lower compared to the yield in the non-irradiated region on the left. This might be again due to ambient light leaking in the fibres reducing the mean light yield.

The lower light yield in the irradiated region of the measurement near the mirror compared to the measurement at 30 cm is due to the increasing expected radiation dose towards the mirror which in turn lead to an increasing attenuation.

Figure 5.8 shows the charge distribution in the irradiated (channel 340-360) and a non-irradiated (channel 200-220) region. The distribution in the irradiated region near the mirror shows a dramatically reduced light yield.

The evolution of the mean light yield as a function of time after the irradiation in the irradiated region is shown in Figure 5.9. These measurements were made one day (*red*), six days (*blue*), 16 days (*green*) and 35 days (*orange*) after the irradiation. Apparently there is a clear sign of a time dependent recovery or an annealing process of the scintillating fibres. Near the mirror the light yield recovers from around 4 p.e. to around 9.5 p.e.. The recovered value for the light yield is in good agreement with the expectations from previous measurements, where no time dependent measurements were made. However, the measured light yield directly

after the irradiation was not expected to be that low.

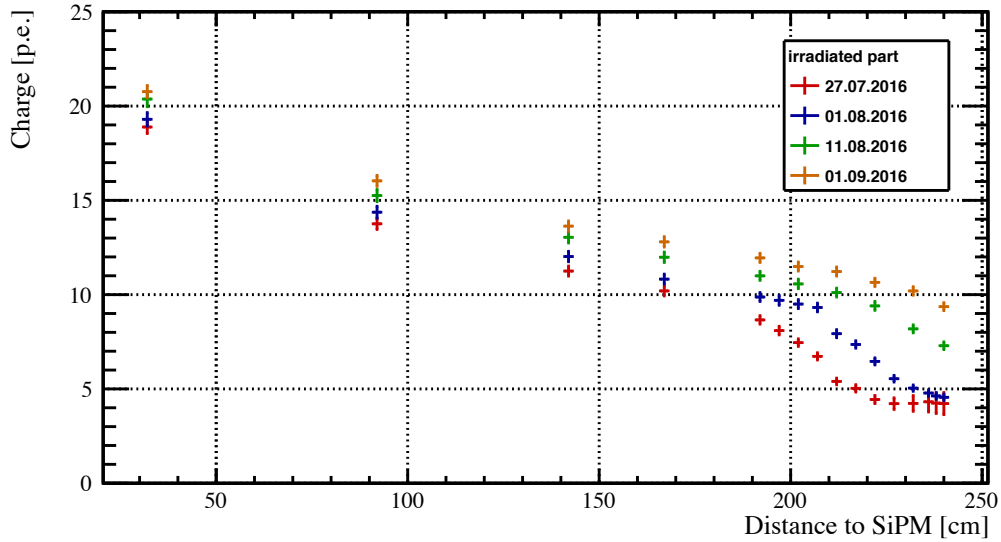


Figure 5.9: Evolution of the mean light yield in the irradiated part along the fibre mat over time. In the the high irradiated part near the mirror the annealing is most intense. Also the limitation due to the cluster algorithm limits the first two measurement runs (*red* and *blue*) near the mirror.

5.3.3 Time Constant

The light yield at the positions 2 cm and 30 cm in front of the mirror is measured on a daily basis, which allows to investigate the time dependence of the annealing for two different dose values. At the 2 cm position the irradiated dose is about 40 kGy whereas the dose at position 30 cm is about 2 kGy (see Figure 5.2).

The evolution of the mean light yield at the centre of the irradiated region over time for the full mat length is plotted in Figure 5.10. The annealing process can be modeled with an exponential function with $L(d)$ the light yield in units of photoelectrons at d days after irradiation:

$$L(d) = L_{\text{perm}} - L_0 e^{-d/\tau}$$

where L_{perm} is the reduced light yield due to the permanent damage of the scintillating fibre, while L_0 is the reduced light yield directly after irradiation and τ is the time constant in units of days. The measurements of the first days near the mirror are biased towards higher values due to the clustering. To exclude the influence of the cluster algorithm due to the low light yield, the fit on the 2 cm position (irradiated with 40 kGy) is restricted to the range starting at 6 days after the irradiation. This leads to a time constant for the annealing of around (12.4 ± 0.7) days.

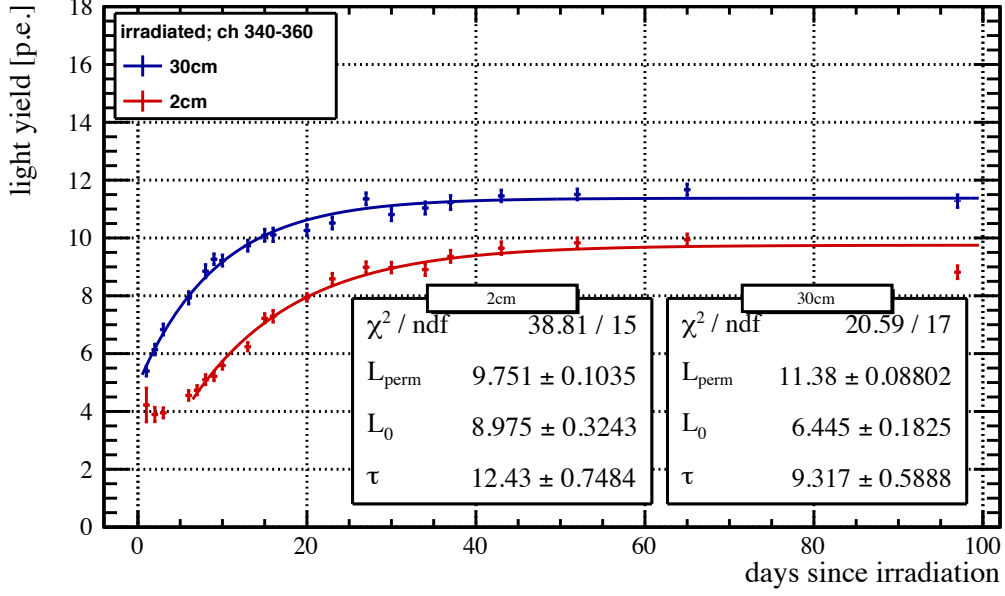


Figure 5.10: Time evolution of the mean light yield at the centre of the irradiated region (channel 340-360) at positions 2 cm (*red*) and 30 cm (*blue*) in front of the mirror. The lines are the fit of an exponential function. The fit parameters (L_{perm} , L_0 , τ) are given in the boxes.

Figure 5.11 shows a reference measurement in the non-irradiated region. The measured light yield varies slightly between measurements, which is most likely due to the temperature dependence of the characteristics of the SiPMs. A linear fit is performed to average the light yield in the non-irradiated region. The light yield near the mirror, as well as 30 cm in front of it, is around 15 p.e..

The loss of light yield after 40 days of annealing near the mirror is about 35% compared to the non-irradiated part. This result is consistent with expectations from previous measurements with single fibres [24]. For the 30 cm position (irradiated with 2 kGy) this fit leads to a time constant for the annealing of around (9.3 ± 0.6) days and a loss of light of about 25% after 40 days of annealing. The obtained time constants indicate a dependency on the radiation dose on the fibre module. However, since the fit of the 2 cm position is excluding the first five days, it is not possible to ensure a dependency on the dose with these measurements.

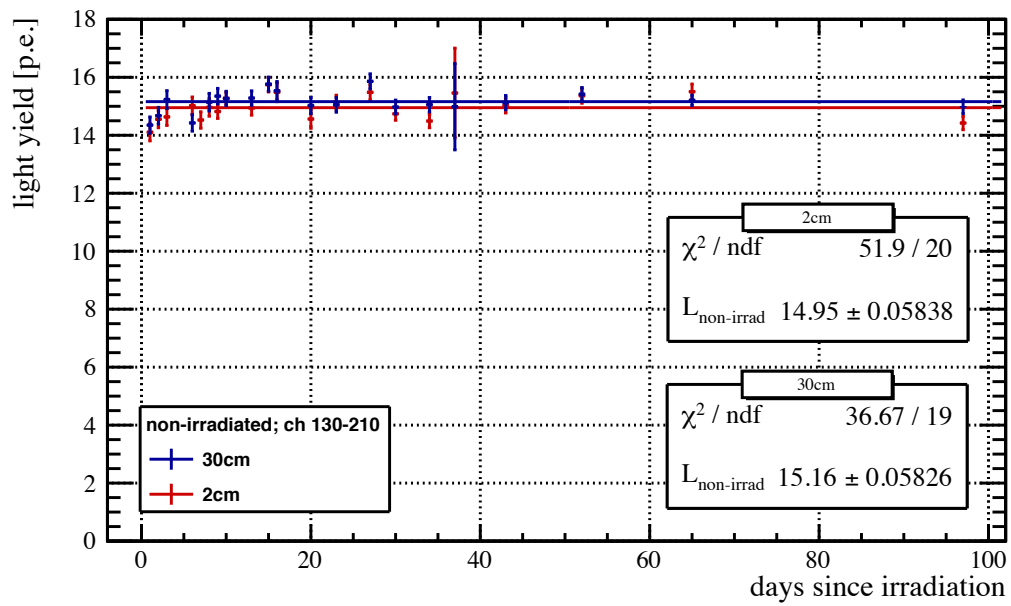


Figure 5.11: Averaged mean light yield of the non-irradiated part (Channel 130-210) monitored over time. The light yield measurement is also slightly dependent on the temperature. A linear fit is performed to average the light yield. Both positions see about 15 photoelectrons.

5.4 Testing with Particle Beam

In order to study the tracking performance of the irradiated module, particle beam measurements have been performed at the North Area of the SPS facility with the H8 beamline at CERN. Around 14 million events have been recorded with two types of beams and with different settings.

5.4.1 Test Beam Setup

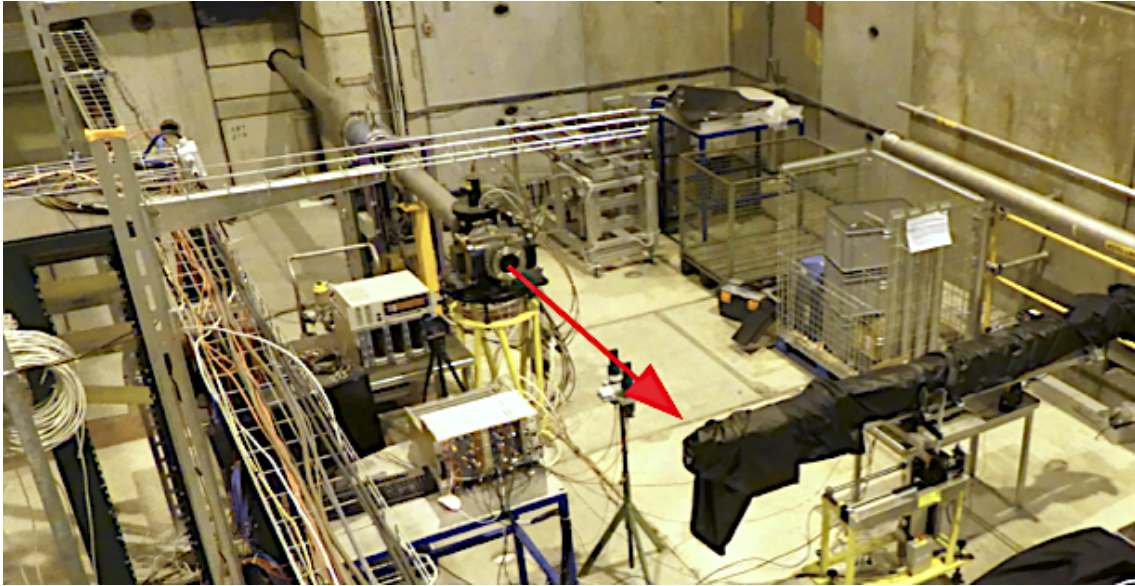


Figure 5.12: Test beam setup with three SciFi test modules covered with black blankets. The red arrow indicates the beam direction.

Figure 5.12 shows the experimental setup of the test beam campaign in November 2016. Three SciFi test modules were placed in the beam line, as shown in Figure 5.13. The outer two modules, the 6-layer 2015 irradiated module and a 2014 5-layer module which was irradiated at the LHCb cavern near the LHC beampipe, were used for track reconstruction. The middle one, the 2016 irradiated module, is used as the DUT (detector under test). The modules were read out by four arrays of SiPMs each which itself are read out by the SPIROC front end boards and the USBBoard DAQ as described in Chapter 4. All data is taken at 3.5 V overvoltage. The trigger for the data acquisition is formed by two scintillators placed in front of the modules. The modules are placed on a two-axes linear table to move the modules during beam time. Due to the narrow beam width, the modules had to be moved in vertical direction to collect enough data over the full width of the fibre modules.

The DUT has been read out with both versions of the Hamamatsu SiPMs, the H2014 and the H2015 version, while the 2015 irradiated module was equipped with the

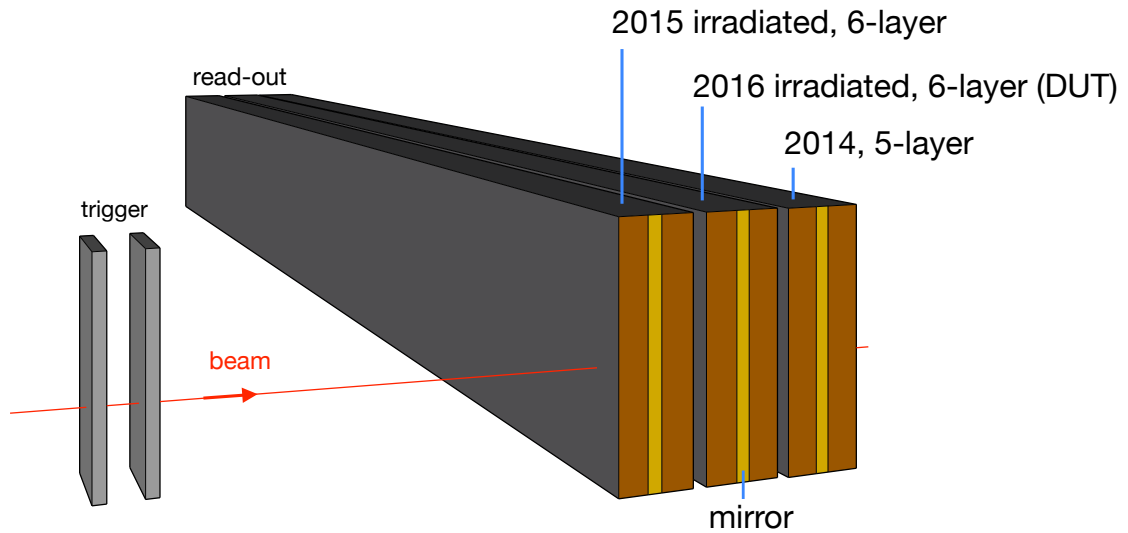


Figure 5.13: Schematic of the setup used during the test beam. All three test modules are placed close to each other with their mirror end inside the beam. Two scintillators are placed in front of the modules as trigger for the DAQ System. The red arrow indicates the beam direction.

H2015 version and the 2014 module, irradiated in the LHCb cavern, was equipped with H2014 arrays. Since the outer two modules were only used for tracking, the SiPMs of these modules were only roughly calibrated.

A mixed beam of protons, pions and muons and a clean muon beam have been used to characterize the modules. The beam properties are described in Chapter 4.

5.4.2 Pre-Analysis & Track Reconstruction

All three test modules have not been aligned very precisely during installation. Therefore a software alignment is done during the analysis. The cluster positions of the outer two tracking modules have been shifted such, that the positions of the clusters match the cluster positions in the DUT. In order to select only clean events the following criteria for the track reconstruction have been used:

- exactly one cluster in each module
- cluster thresholds: seed 2.5 , neighbour 1.5 , sum 4.5
- width of clusters smaller than 5 channels
- relative position of clusters within 1 mm after alignment

5.4.3 Light Yield

The light yield of the 2016 irradiated test module (DUT) has been measured using a mixed pion beam, a muon beam and both types of Hamamatsu SiPMs (H2014, H2015). Three different configurations have been used. While the pion beam was measured only with the H2014 Hamamatsu SiPM arrays, the muon beam has been measured with the H2015 version as well. The collected charge distributions for the three measurement runs are shown in Figure 5.14. The top row shows the collected charge in units of p.e. in the non-irradiated region between channel 260 and 440, whereas the bottom row shows the corresponding irradiated part, between channel 150 and channel 170. The channels next to the gaps of the SiPM dies have been excluded. The mean light yield of the non-irradiated as well as the irradiated part is given in Table 5.1.

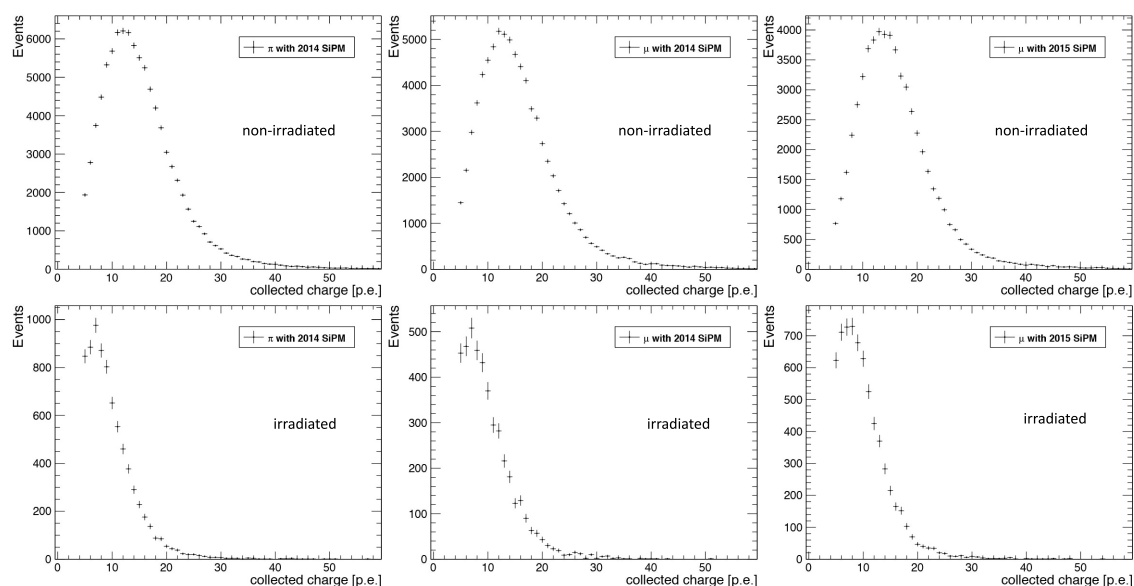


Figure 5.14: Collected charge distribution measured with pion beam and H2014 SiPMs (left), muon beam and H2014 SiPMs (centre) and with muon beam and H2015 SiPMs (right).

Table 5.1: Average light yield of all three measured configurations in the non-irradiated and in the irradiated part in units of photoelectrons [p.e.].

	π -beam H2014 SiPM	μ -beam H2014 SiPM	μ -beam H2015 SiPM
non-irradiated	(15.30 ± 0.31) p.e.	(15.74 ± 0.36) p.e.	(16.10 ± 0.39) p.e.
irradiated	(9.94 ± 0.24) p.e.	(10.28 ± 0.33) p.e.	(10.31 ± 0.26) p.e.

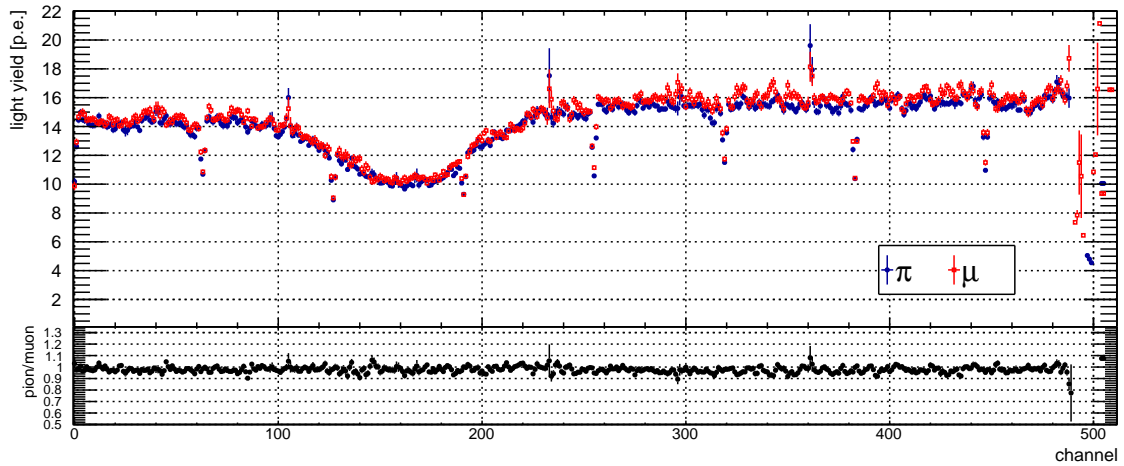


Figure 5.15: Comparison of light yield measurements of muon and pion beam measured with Hamamatsu H2014 SiPM arrays.

π -beam vs μ -beam. Figure 5.15 shows the comparison of the mean light yield in each channel measured with the pion and the muon beam with the H2014 SiPM arrays. The missing entries on the right edge are due to the misalignment of the three modules. Since the DUT was slightly shifted compared to both tracking modules no tracks have been reconstructed in this region. As one would expect, the difference in the photon yield between muon and pion beam is small since both particles have nearly the same mass and the same energy.

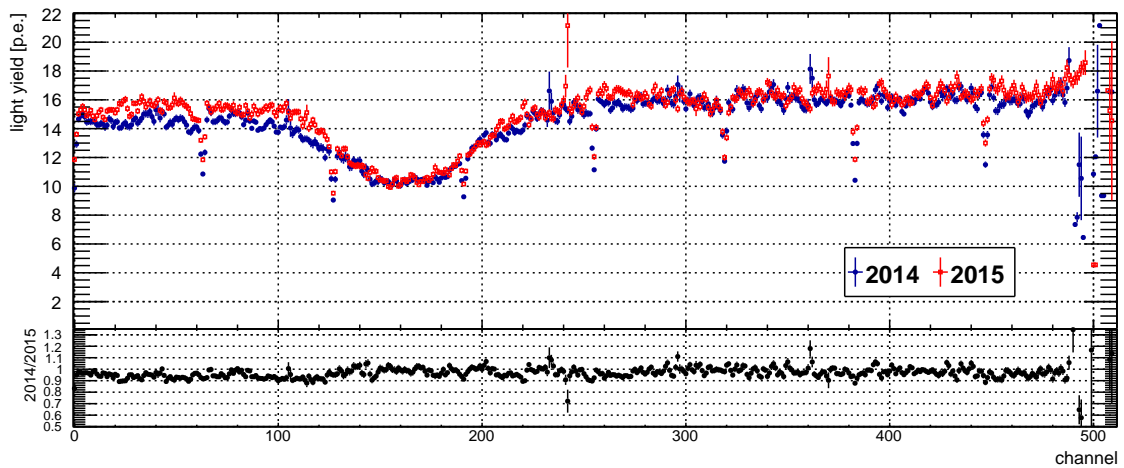


Figure 5.16: Comparison of light yield measurements made with both versions of the SiPM arrays with the muon beam.

H2014 vs H2015 SiPM arrays. The comparison between both SiPM versions with the muon beam is shown in Figure 5.16. The right side of the plot, starting in

the irradiated region around channel 160, shows a similar light yield for both SiPM version, whereas the left side shows a 1-2 p.e. higher yield for the H2015 arrays. Due to the higher PDE of 47% of the H2015 version compared to the PDE of 39% of the H2014 version (see Table 4.1) one would expect a 2-3 p.e. higher light yield with the H2015 arrays. Due to a higher cross-talk ($\sim 12\%$) in the H2014 arrays, fake signals could increase the light yield of the H2014 SiPM. Due to a smaller active area of the H2014 SiPM arrays, the probability of a misalignment of the arrays to fibre matrix is increased. This could explain the lower light yield on the left side of the H2014 measurement, since only the first SiPM (channel 1 to 128) is affected.

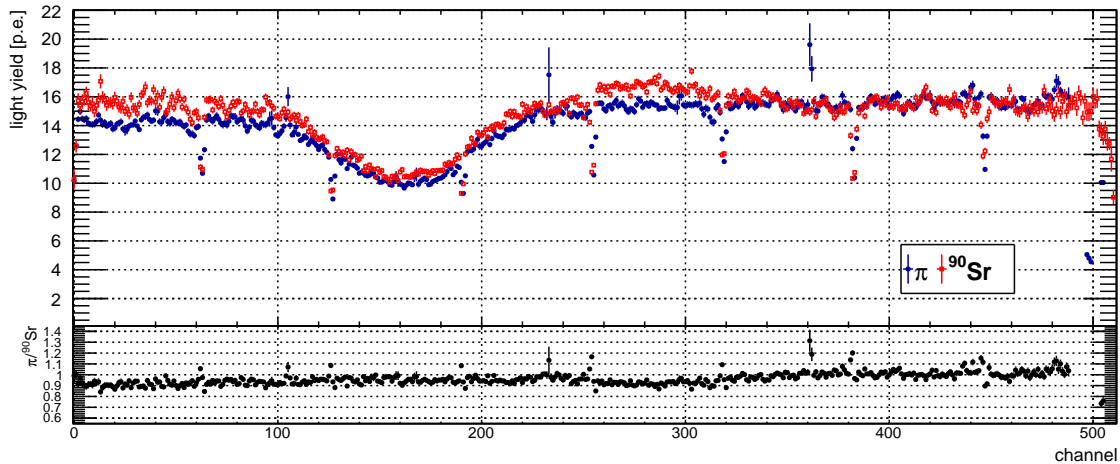


Figure 5.17: Comparison of the light yield measured with pion beam and with the ^{90}Sr setup, both measured with H2014 arrays.

π -beam vs ^{90}Sr source. The comparison of the mean light yield per channel of the pion beam measurement with the lab measurement done with the ^{90}Sr source is shown in Figure 5.17. The clustering of the ^{90}Sr measurement was using the cluster thresholds used for the test beam data. From channel 256 to channel 384 the ^{90}Sr measurement shows a small slope which could be explained by a small misalignment of the SiPMs compared to the fibres. Since the H2014 SiPM version arrays have a smaller active area, compared to the H2015 version, it is more likely that the active area does not cover the full fibre matrix. However, this comparison confirms the choice of ^{90}Sr source for quality assurance measurements.

Cluster size. The cluster size is shown in Figure 5.18. The comparison of the cluster size measured with the pion and the muon beam and H2014 SiPMs is within their statistical uncertainties the same, at around 2.5 channels per cluster. The comparison between the H2014 and the H2015 SiPM arrays shows that the H2015 arrays have more narrow clusters with a mean of 2.21 channels per cluster. This is probably due to the fact, that the H2015 version has a reduced cross-talk ($\sim 12\%$) between the channels.

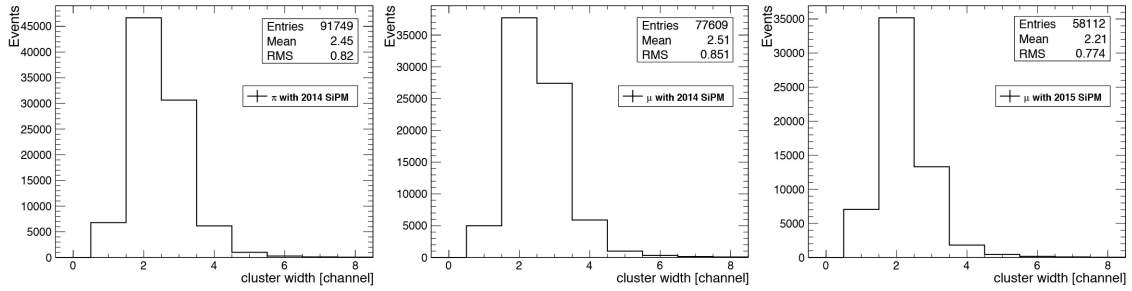


Figure 5.18: Cluster size distribution measured with pion beam and H2014 SiPMs (left), muon beam and H2014 SiPMs (centre) and with muon beam and H2015 SiPMs (right).

5.4.4 Hit Efficiency

The single hit efficiency is determined by counting how often a particle hitting the module cause a signal which passes the applied cluster thresholds. The hit position of the track in the DUT is again determined by the track reconstruction with the outer two modules. The efficiency is determined for two different sum thresholds of the applied clustering algorithm. The seed and neighbour threshold are kept at 2.5 p.e. and 1.5 p.e. respectively.

Figures 5.19 and 5.20 are showing the single hit efficiency in each channel measured near the mirror with the H2015 SiPM arrays and the H2014 SiPM arrays, respectively. The efficiencies for the non-irradiated (channel 260-300) and the irradiated (channel 150-170) region are obtained by a constant fit in the corresponding channel range. The results are given in Table 5.2. Using the H2015 SiPM arrays and clustering with the sum threshold of 4.5 p.e., the hit efficiency near the mirror in the non-irradiated region is $(98.38 \pm 0.12)\%$ and decreases to $(85.13 \pm 0.58)\%$ in the irradiated region. By lowering the sum threshold to 2.5 p.e., the single hit efficiency near the mirror increases to $(99.22 \pm 0.09)\%$ in the non-irradiated and $(94.17 \pm 0.41)\%$ in the irradiated region respectively.

Using the H2014 SiPM arrays and the 4.5 sum threshold, the efficiencies near the mirror are $(96.71 \pm 0.16)\%$ in the non-irradiated and $(79.95 \pm 0.81)\%$ in the irradiated region. With a lower sum threshold the efficiencies increase as well to $(98.50 \pm 0.11)\%$ and $(90.75 \pm 0.59)\%$.

The comparison of the two SiPM arrays shows a clear gain in efficiency for the newer H2015 version of up to 5% in the irradiated region at low light yield. By lowering the sum threshold of the cluster algorithm the efficiencies increase significantly.

The single hit efficiency as a function of the light yield for the muon beam using the H2015 SiPM arrays and two different cluster sum thresholds is shown in Figure 5.21. The light yield dependence of the efficiency was found to be modeled by an exponential function in the form:

$$\epsilon(x) = 1 - a e^{bx},$$

Table 5.2: Efficiencies obtained in the non-irradiated and the irradiated region near the mirror with H2015 and H2014 SiPM arrays and two different sum thresholds (4.5 p.e., 2.5 p.e.).

SiPM	sum	non-irradiated	irradiated
H2015	4.5	$(98.38 \pm 0.12)\%$	$(85.13 \pm 0.58)\%$
H2015	2.5	$(99.22 \pm 0.09)\%$	$(94.17 \pm 0.41)\%$
H2014	4.5	$(96.71 \pm 0.16)\%$	$(79.95 \pm 0.81)\%$
H2014	2.5	$(98.50 \pm 0.11)\%$	$(90.75 \pm 0.59)\%$

where ϵ is the efficiency, x is the light yield and a and b are constants. Figure 5.22 shows the corresponding plot for the H2014 SiPM arrays. The difference in clustering with a lower sum threshold is significantly, especially in the low light yield region.

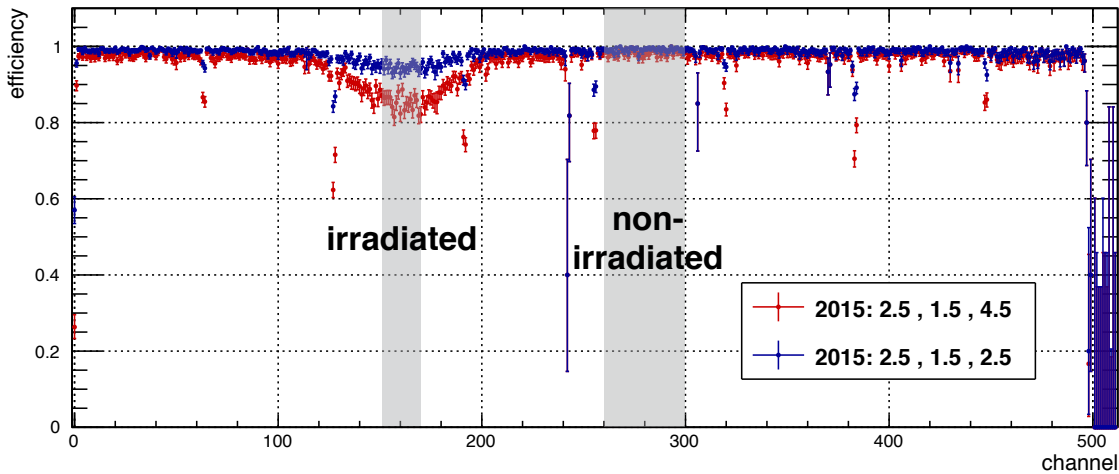


Figure 5.19: Single hit efficiency for each channel measured with the H2015 SiPM arrays. Irradiated and non-irradiated regions are highlighted in grey. The efficiencies in the region above channel 500 couldn't be determined due to missing tracks of the tracking modules.

5.5 Summary

An irradiated test module has been characterized directly after its irradiation with a mixed pion beam at CERN. The measurement showed an unexpectedly large signal

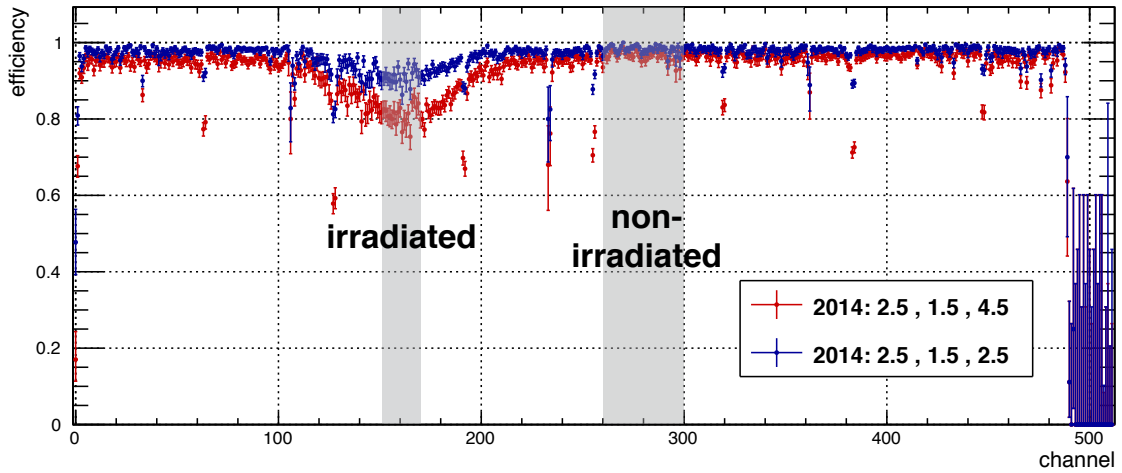


Figure 5.20: Single hit efficiency for each channel measured with the H2014 SiPM arrays.

loss in the irradiated region. When the light yield measurement was redone several months later, a recovered light yield was measured, which matched the expectations from previous irradiation tests. To investigate whether this is a time dependent effect, another test module has been irradiated at CERN and investigated as a function of time starting directly after irradiation.

The measurements near the mirror showed again a large signal loss in the irradiated region, with a light yield of around 4 p.e.. It turned out, that the light yield in the irradiated region is biased to higher values because the cluster algorithm exclude events with a cluster charge lower than the 2.5 p.e. sum threshold. After 6 weeks the light yield near the mirror in the irradiated region (40 kGy) recovered to around 9.5 p.e., which is within the expectation from previous studies. Excluding the first five days due to the influence of the cluster algorithm on low light yield, a time constant of (12.4 ± 0.7) days was calculated. The light yield, measured in a less irradiated region (2 kGy) at 30 cm in front of the mirror, recovered in the same time from 5.5 p.e. to 11.5 p.e. with a time constant of (9.3 ± 0.6) days. The comparison of the two time constants obtained at different positions irradiated with different doses indicate a dose dependency of the time constant of annealing. Since the calculation of the time constant in the high irradiated region is excluding the first five days after irradiation, further investigations are necessary to ensure this dependency.

Measurements of the single hit efficiency near the mirror of the irradiated test module have been performed in a muon beam. By using the H2015 SiPM arrays and the cluster threshold of 2.5 p.e. for seed, 1.5 p.e. for neighbour and 4.5 p.e. for sum, the hit efficiencies were calculated, resulting in $(98.38 \pm 0.12)\%$ in the non-irradiated region. In the irradiation with the expected lifetime dose, the efficiency near the mirror decreases in the irradiated region to $(85.13 \pm 0.58)\%$. To maintain a high

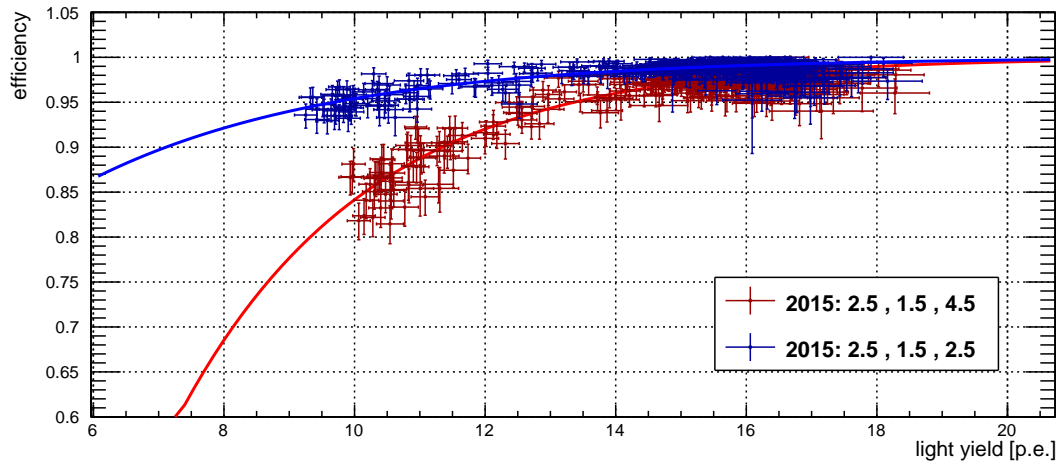


Figure 5.21: Single hit efficiency measured with the H2015 SiPM arrays for two different sum thresholds (4.5 p.e., 2.5 p.e.).

hit efficiency during the lifetime of the detector, the cluster thresholds have to be adjusted. By lowering only the sum threshold to 2.5 p.e., the hit efficiency near the mirror will increase by nearly 10% in the irradiated region to $(94.17 \pm 0.41)\%$.

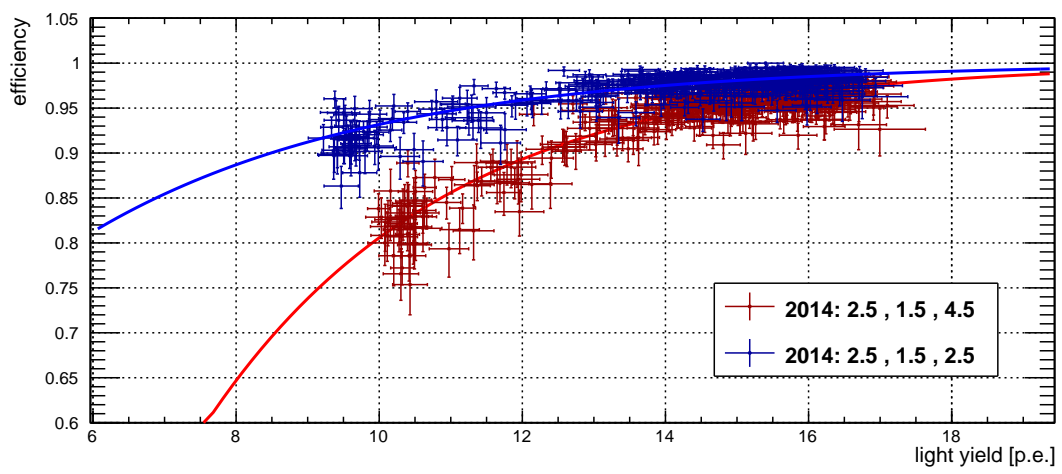


Figure 5.22: Single hit efficiency measured with the H2014 SiPM arrays for two different sum thresholds (4.5 p.e., 2.5 p.e.).

6 Quality Checks for Serial Production of Fibre Mats and Modules

To ensure a high tracking detector performance for charged particles, it is necessary to monitor the fibre mat quality during the serial production. Therefore ^{90}Sr source measurements of the light yield near the mirror are done before and after a critical production step as for example the longitudinal cut. After assembling the fibre mats to modules the light yield of the full module is also measured using cosmic rays, to cross check if the fibre mats have been damage during the assembly.

6.1 Fibre Mats

After receiving the fibre mats from the mat winding centres, the light yield of the mats is measured in order to compare it later to the measurement done after the critical longitudinal cut. These measurements are done using the experimental setup described in Chapter 4 using H2014 and H2015 SiPM arrays with a ^{90}Sr source placed 13 cm in front of the mirror.

The light yield of a single fibre mat (*FIM00075*) is shown in Figure 6.1. Apart from the known dips every 64 channels due to the gaps of the SiPMs and an additional dip due to one broken SiPM channel, the fibre mat has no further damages. The fibre mat *FIM00075* has an very homogeneous light yield over the full width of the mat of (18.76 ± 0.26) p.e. in average. Compared to the measurements in the previous chapter, this fibre mat has a higher light yield. The increase is due to an improvement of the fibre quality by the producer (Kuraray).

6.1.1 Attenuation Length

The attenuation length of the scintillating fibres is determined by measuring the averaged mean light yield for multiple positions along the fibre mat. The light yield dependence on the distance to the SiPMs is modeled by a double exponential as described in Chapter 3. With $N(x)$ being the mean number of detected photoelectrons at distance x :

$$N(x) = N_L e^{-x/\lambda_L} + N_S e^{-x/\lambda_S}$$

where λ_L and λ_S are the attenuation lengths of the long and short components, respectively. N_L and N_S are the number of photoelectrons as seen by a SiPM at distance zero (at the position of the source) for each component.

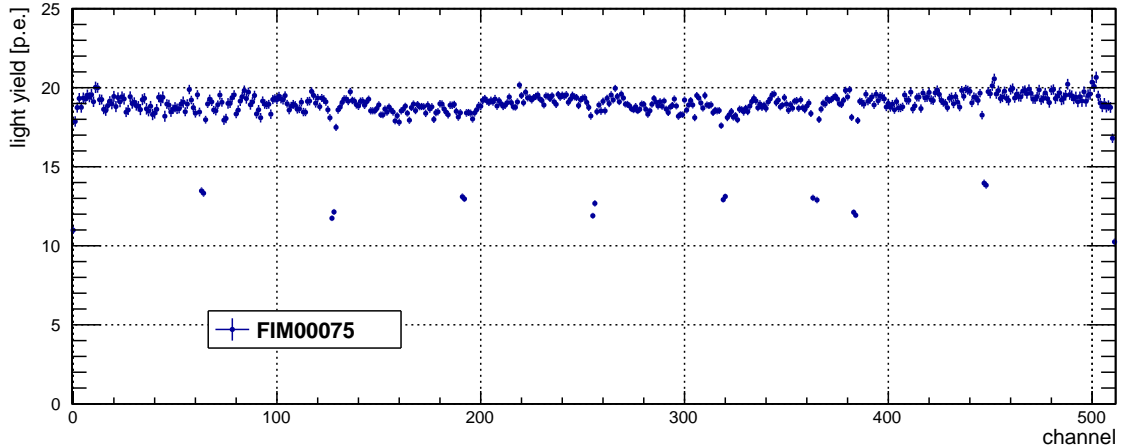


Figure 6.1: Light yield of a single fibre mat before executing the critical longitudinal cut. The light yield is distributed very homogeneous over the full width of the mat. As expected, there is the drop in light yield due to the gaps of the SiPMs every 64 channels. Additional gap due to broken SiPM channel around channel 370.

Figure 6.2 shows the attenuation measurement for fibre mat *FIM00036*. This fibre mat was measured without an assembled mirror. This leads to a decreased light yield near the mirror of around 9-10 photoelectrons. However this allows to determine the attenuation length. The length can not easily be determined with an assembled mirror, because the fit needs to account for the fraction of reflected light. The measurements of the long and short components of the attenuation length on *FIM00036* resulted in (371.6 ± 21.1) cm and (40.17 ± 8.90) cm, respectively.

6.1.2 Gain of the Mirror

The gain of using a mirror at the fibre end can easily be measured by taking the ratio of a measurement made with and without the mirror. Figure 6.3 shows the mean light yield of the measurements with and without the mirror of fibre mat *FIM00036*. The reflectivity can be obtained from the ratio plot on the bottom which shows a gain in light yield of around 80% as expected from previous mirror studies [9].

6.1.3 Longitudinal Cut

In order to achieve a uniform fibre matrix inside the fibre mats, the mats are wound slightly wider than needed (see Figure 3.7). To avoid damage on the edge of the fibre mats during the transportation from the mat winding centres to the module production centres, the longitudinal cut of the fibre mats to the correct width is performed at the module production institutes. This cut has to be done with a precision of $150 \mu\text{m}$ over the 2,42 m long fibre mat in order to ensure the needed tolerance

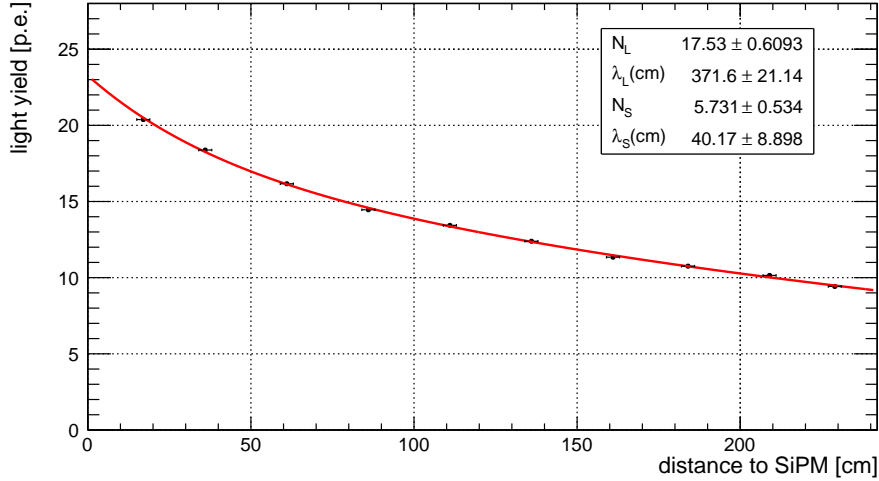


Figure 6.2: Mean light yield of *FIM00036* at different positions along the fibre mat. The red line shows a double exponential fit.

between the mats during module production. Therefore the fibre mat is aligned on an aluminium template using the alignment pins of the mat as shown in Figure 6.4. The cut itself is done with a circular saw on a professional milling machine. This machine efficiently removes the cut excess and provides a reasonable cooling due to the good thermal conductivity of the blade to avoid additional damage.

Nonetheless this cut can introduce two different damages to the fibre mat. If the mat is not strictly straight but curved, the cut can damage multiple fibres on the edges causing a larger drop in light yield. Additionally the mirror glued at the end of the fibre mat can be damaged during the cut. The circular rotating blade exert pressure on the mirror which can lead to a peeling-off of the mirror at the edges.

Unfortunately the clustering algorithm introduces lower light yield on the edges due to the missing charge of the neighbouring channels. To avoid this and to point out the effect of the longitudinal cut on the outermost channels, a different method of calculating the light yield is used. Instead of performing a full clustering algorithm a simple single channel noise rejection threshold is set.

The resulting single channel light yield for *FIM00073* is shown in Figure 6.5. The top shows both measurements before and after the longitudinal cut while the bottom shows the ratio of these. The single channel light yield distribution has a convex shape across all the channels due to the position of the beta source. The particles which are passing the fibre mat on the edges have a larger angle which in turn leads to a broader charge distribution and therefore in average a reduced charge per channel. In the centre of the fibre mat, where the particles passing straight through, the charge distribution is much more narrow. By using the single channel light yield, features like the gaps due to the SiPM dies and arrays have vanished, since the algorithm is not including the charge of the neighbouring channels anymore.

In order to inspect the quality of the longitudinal cut, photographs of the edges of

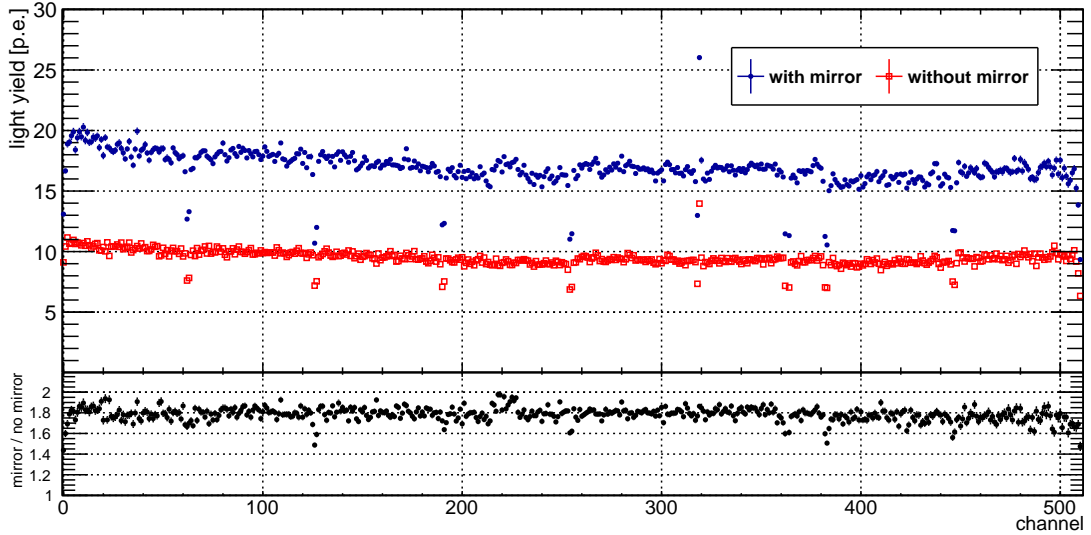


Figure 6.3: Mean light yield of FIM00036 with and without mirror. The bottom plot shows the ratio of both measurements.

the mats are taken with an high resolution camera. Figure 6.6 shows a detailed plot of the single channel ratio on the edges as well as the corresponding optical images. On the left side one can see that the outer two fibres in each layer are affected (black fibres) while on the right side only the outermost fibres suffer from the longitudinal cut. The same is visible in the single channel light yield. Since the outermost fibre is outside of the active area of the SiPMs there is nearly no effect on the light yield, whereas the left side in Figure 6.6 shows a loss of nearly 40% due to more fibres being damaged. Since the loss is about 40% it is most likely that the damage is due to a peeling-off of the mirror rather than a damage on the fibres itself. One would expect that a damage of the fibres would lead to a nearly complete loss of light. A histogram of the number of bad channels for each mat is shown in Figure 6.7. The bad channels on the left and right side are summed. A bad channel is defined as a channel on the edge with a ratio below 80% between the cut and uncut measurement. The histogram contains the last 54 fibre mats of the early serial production. Less than 4% are showing a significant damage, where more than two channels have a ratio below 80%.



Figure 6.4: *Left*: Picture of the milling machine with the aluminium jig for the longitudinal cut. *Right*: Detailed view of the template with a rail system to extend the range of the machine to 2.5 m. [9]

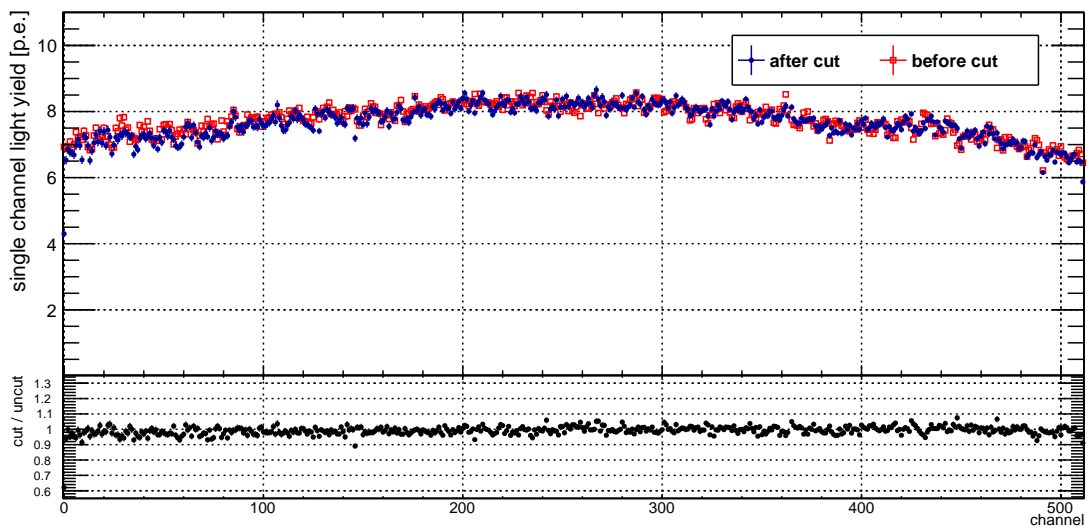


Figure 6.5: Single channel mean light yield of *FIM00073* before and after the longitudinal cut.

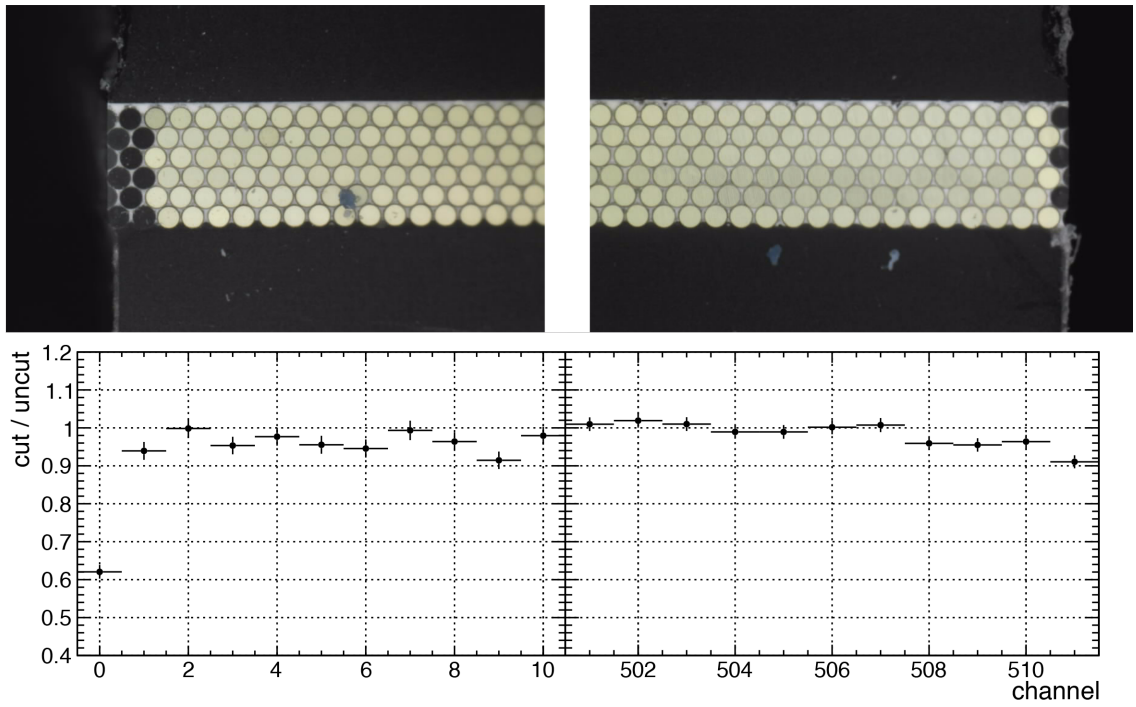


Figure 6.6: *Top*: Photograph of the edges of *FIM00073* after the longitudinal cut. *Bottom*: Single channel light yield ratio in the corresponding region.

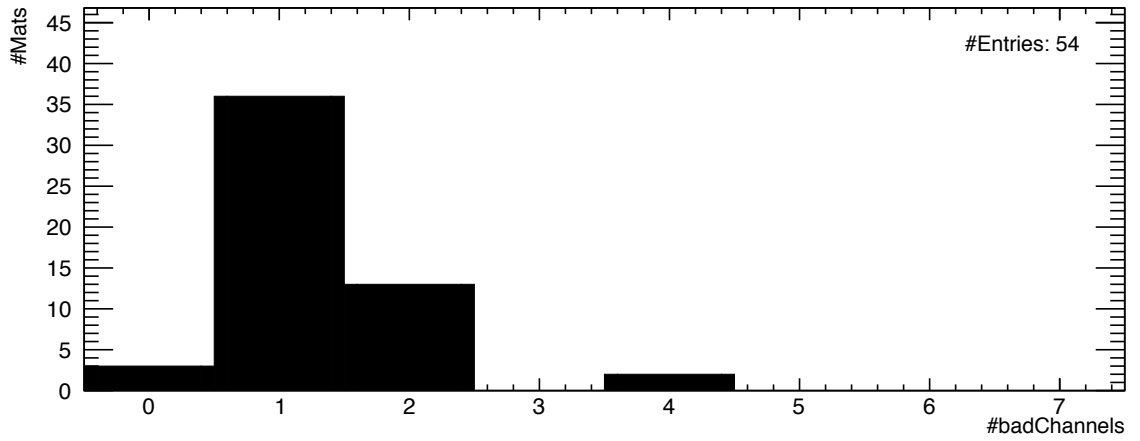


Figure 6.7: Histogram of the number of channels which have a light loss of at least 20% in the channels near the edges of the last 54 fibre mats during serial production.

6.2 Fibre Modules

After the fibre mats are cut and measured with the ^{90}Sr source, eight of them are assembled together to one full size module. In order to see if damages occurred during the assembly of the module it is necessary to measure the light yield after the module is finished. Due to radiation safety concerns for the lab where the modules are assembled and tested, the measurement is done using cosmic muons instead of beta electrons. Figure 6.8 shows the module test setup. The read out consist now of 2×2048 channels of the H2015 SiPM version and is triggered by a large scintillator near the mirror on each module side. Each trigger leads to a read-out of both module sides.



Figure 6.8: Full size fibre module measurement setup. Both ends are covered with black blankets. Two large scintillator paddle trigger are placed near the mirrors for each of the module sides.

The resulting single channel light yield for each channel for one of the early full modules produced (*FSM00008*) is shown in Figure 6.9. The top part shows one side of the module (Side A), the bottom shows the second side of the module (Side B) respectively. Additionally the equivalent ^{90}Sr measurements of the single mats done before are shown in red. The ratio between both measurements is plotted below. First of all, the measurement using cosmic rays shows a rather homogeneous single channel light yield distribution over all channels of around 8 p.e.. Since the cosmic muons passing the fibre module in a large variety of angles in every channel, the single channel light yield has a flat shape unlike the ^{90}Sr measurement. Some channels of the cosmic muon measurement are showing a very high light yield, which are caused by a bad calibration of the SiPM channels.

By plotting the ratio of both measurements one can easily see if there have been additional damages introduced during module production, especially on the edges on

the fibre mats. On *FSM00008* the edges between two adjacent fibre mats, located around channels 512, 1024 and 1536, show nearly no impact of the production process. Only the channels 1024 and 1025 on module side B, which are corresponding to the edge between the two centred mats, are showing a loss of around 20% of light.

6.3 Summary

In this chapter several quality checks of the fibre module production were presented. The long and short components of the attenuation length of a scintillating fibre mat have been measured with (371.6 ± 21.1) cm and (40.17 ± 8.90) cm respectively. The gain in light yield of using the mirror was found to be around 80%. The light yield of each fibre mat used for the module production is measured before and after the execution of the longitudinal cut. Less than 4% of the last 54 mats investigated showed a damage on the outer edges of the fibre mat where only few channels are affected due to a peeling-off of the mirror.

Light yield measurements using cosmic rays have been made to investigate the full size fibre modules after production. Especially the edges between two adjacent fibre mats are checked for additional damage which occurred during the production process. The latest production module showed only a small visible influence of the production process.

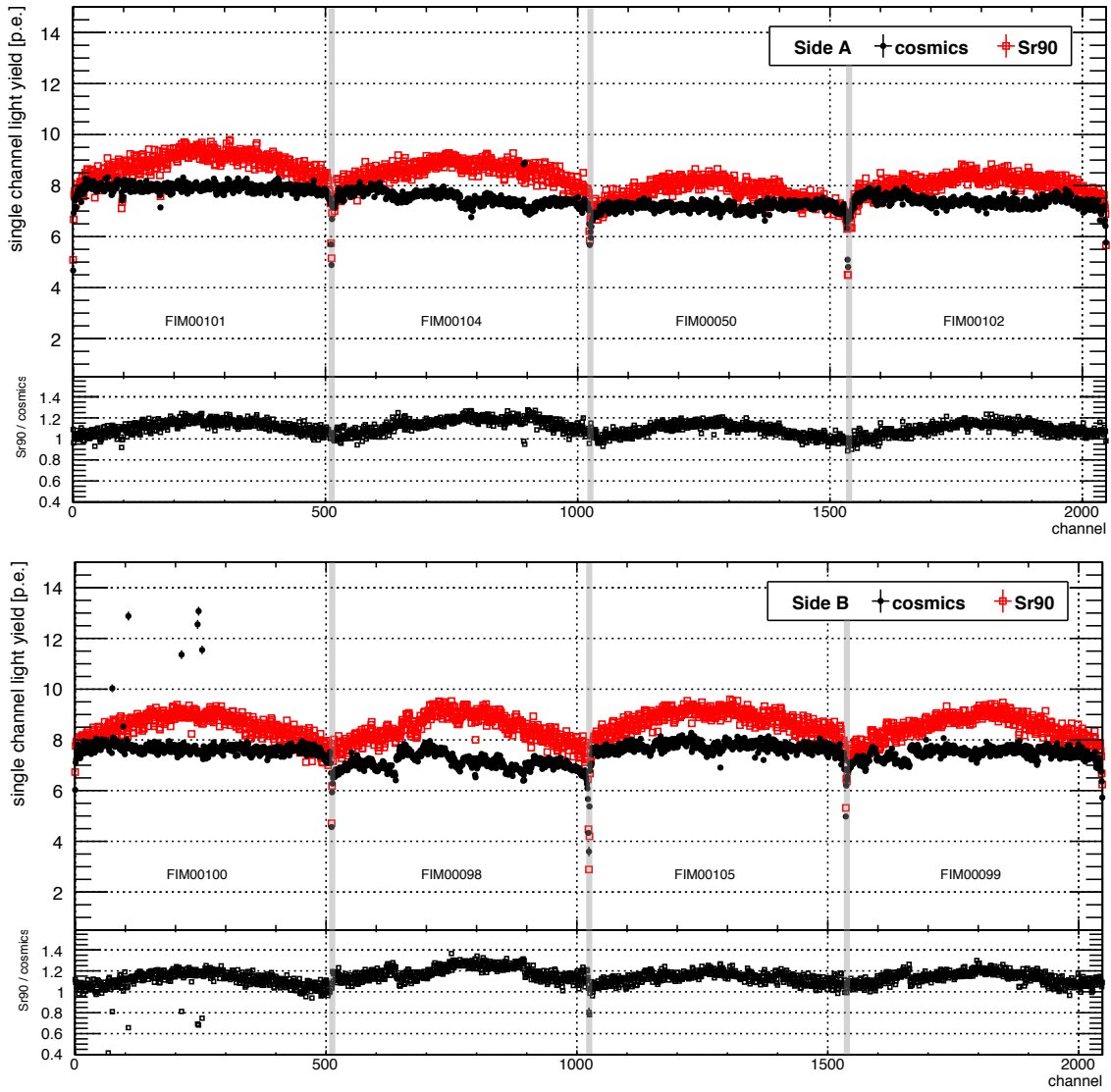


Figure 6.9: Single channel light yield measurement using cosmic muons of full size module *FSM00008*. The edges between two adjacent fibre mats are highlighted in grey. *Top*: Comparison of cosmic measurement (*black*) with the ^{90}Sr measurement (*red*) for module side A. *Bottom*: Comparison for module side B.

7 Conclusion

During LHC's Long Shutdown 2 beginning in 2019, an upgrade of the current tracking system of the LHCb experiment will take place. To replace the existing main tracker a new Scintillating Fibre Tracker (SciFi Tracker) has been developed, using scintillating fibres as the active element of the detector. The fibres are wound to six-layer fibre mats and afterwards assembled to modules containing 8 fibre mats. The modules are arranged in 12 planes containing 10 to 12 modules each. The scintillation light of each module is read out with 32 multi-channel silicon photomultiplier (SiPM) arrays (4096 channels per module). Due to a non-uniform radiation environment, the scintillating fibres suffer from radiation damage by ionizing particles, highly dependent on their position inside the detector.

This thesis presented studies of irradiated fibre modules. The light yield of an irradiated test module has been investigated as a function of time and characterized in a particle beam. Therefore a single fibre mat test module was irradiated at CERN with the expected lifetime dose of the LHCb detector. Light yield measurements have been performed on a daily basis starting directly after the irradiation. These measurements revealed an annealing time constant of (12.4 ± 0.7) days in a high irradiated region with a dose of around 40 kGy. The light yield recovered within six weeks to 65% of the light yield before irradiation. The annealing time constant in a region irradiated with 2 kGy has been found to be (9.3 ± 0.6) days, reaching a light yield of 75% of the light yield before irradiation after six weeks of annealing.

Measurements of the newly irradiated module in a particle beam are presented as well. Comparisons of the mean light yield near the mirror of two different particle beams and two different SiPM versions are showing only small differences. Additionally the comparison of the particle beam measurements with a ^{90}Sr lab measurement confirms the choice of the ^{90}Sr source for quality assurance measurements. The hit efficiency of the irradiated detector is calculated. Using the suggested nominal thresholds of 2.5 p.e. for seed, 1.5 p.e. for neighbour and 4.5 p.e. for the sum, a single hit efficiency of $(98.38 \pm 0.12)\%$ in the non-irradiated region is reached. In the irradiated region, the hit efficiency decreases to $(85.13 \pm 0.58)\%$. By lowering the sum threshold to 2.5 p.e., the efficiencies increase to $(99.22 \pm 0.09)\%$ and $(94.17 \pm 0.41)\%$, respectively.

Additionally several quality checks are done before and especially during the start of the serial production. The attenuation length of the scintillating fibres is measured using the ^{90}Sr setup resulting in (371.6 ± 21.1) cm for the long and (40.17 ± 8.90) cm for the short component. A light yield measurement of a fibre mat with and

without a mirror showed a maximum gain of around 80% near the mirror. After performing the longitudinal cut, light yield measurements are repeated concerning the light yield on the edges of the fibre mats. Less than 4% of the cut fibre mats of the early serial production showed damages, where up to 4 channels on the edges have a loss of light of more than 20% due to a peeling-off of the mirror. Finally the full size fibre modules are undergoing again a light yield measurement using cosmic rays. The results are compared to the ^{90}Sr measurements to see if additional damages on the edges of the fibre mats occur during the module production. The test so far could not reveal serious damages introduced during the module assembly.

Part I
Appendix

A Bibliography

- [1] Oliver Sim Brüning, Paul Collier, P Lebrun, Stephen Myers, Ranko Ostojic, John Poole, and Paul Proudlock. *LHC Design Report*. CERN, Geneva, 2004. URL <https://cds.cern.ch/record/782076>.
- [2] AC Team. *The four main LHC experiments*. 1999. URL <http://cds.cern.ch/record/40525>.
- [3] URL http://www.quantumdiaries.org/wp-content/uploads/2014/03/2000px-Standard_Model_of_Elementary_Particles.svg_.jpg.
- [4] LHCb Tracker Upgrade Technical Design Report, 2014. LHCb-TDR-015.
- [5] Framework TDR for the LHCb Upgrade: Technical Design Report, 2012. LHCb-TDR-012.
- [6] K. Henessy. Nuclear instruments & methods in physics research a: Lhcb velo upgrade. *ELSEVIER*, 2016.
- [7] LHCb PID Upgrade Technical Design Report, 2013. LHCb-TDR-014.
- [8] LHCb Trigger and Online Technical Design Report, 2014. LHCb-TDR-016.
- [9] Christian Joram, Ulrich Uwer, Blake Dean Leverington, Thomas Kirn, Sebastian Bachmann, Robert Jan Ekelhof, and Janine Müller. LHCb Scintillating Fibre Tracker Engineering Design Review Report: Fibres, Mats and Modules. Technical Report LHCb-PUB-2015-008. CERN-LHCb-PUB-2015-008, CERN, Geneva, Mar 2015. URL <https://cds.cern.ch/record/2004811>.
- [10] N. Lopez March and M. Karacson. Radiation studies for the LHCb tracker upgrade. Technical Report LHCb-PUB-2014-022, CERN-LHCb-PUB-2014-022, LHCb-INT-2013-003, Jan 2013.
- [11] A. Fasso et al. FLUKA: a multi-particle transport code, 2005. CERN-2005-10, INFN/TC05/11, SLAC-R-773.
- [12] G. Battistoni et al. The FLUKA code: Description and benchmarking. In M. Albrow and R. Raja, editors, *Proceedings of the Hadronic Shower Simulation Workshop 2006*, AIP Conference Proceeding 896, pages 31–49, 2007.
- [13] Kuraray Plastic Scintillating Fibres, 2014. URL <http://kuraraypsf.jp/psf/sf.html>. as specified on the Kuraray web site: <http://kuraraypsf.jp/psf/sf.html>.

- [14] Aurelio Bay, Frederic Blanc, Sebastian Bruggisser, Olivier Callot, Hervé Chanal, E Cogneras, Albert Comerma-Montells, Mirko Deckenhoff, Gerard Decreuse, Moritz Demmer, Victor Egorychev, Robert Ekelhof, David Gascon, Andrei Golutvin, Eugeni Graugès, Oliver Grünberg, Evgeny Gushchin, Yury Guz, Guido Haefeli, Pierre Jatou, Christian Joram, Matthias Karacson, Blake Leverington, Rolf Lindner, Neus Lopez-March, Tatsuya Nakada, Mitesh Patel, Pascal Perret, Albert Puig Navarro, Barinjaka Rakotomiaramanana, Julien Rouvinet, Trevor Savidge, Olivier Schneider, Thomas Schneider, Pavel Shatalov, Bernhard Spaan, Eric Thomas, Giovanni Veneziano, Ulrich Uwer, Zhirui Xu, and Hao Yu. Viability Assessment of a Scintillating Fibre Tracker for the LHCb Upgrade. Technical Report LHCb-PUB-2014-015. CERN-LHCb-PUB-2014-015. LHCb-INT-2013-004, CERN, Geneva, Feb 2014. URL <http://cds.cern.ch/record/1662525>.
- [15] T.O. White. Scintillating fibres. *Nucl.Instrum.Meth.*, A273:820–825, 1988. ISSN 0168-9002. doi: [http://dx.doi.org/10.1016/0168-9002\(88\)90102-7](http://dx.doi.org/10.1016/0168-9002(88)90102-7). URL <http://www.sciencedirect.com/science/article/pii/0168900288901027>.
- [16] J.B. Birks. *The Theory and Practice of Scintillation Counting*. Pergamon, 1964.
- [17] Joseph R. Lakowicz. *Principles of Fluorescence Spectroscopy*. Springer, 2006.
- [18] A.E. Baulin et al. Attenuation length and spectral response of kuraray scsf-78mj scintillating fibres. *Nucl. Instr. Meth. Phys. Res. A*, 2013.
- [19] W. Busjan, K. Wick, and T. Zoufal. Shortlived absorption centers in plastic scintillators and their influence on the fluorescence light yield. *Nuclear Instruments and Methods in Physics Research Section B: Beam Interactions with Materials and Atoms*, 152(1):89 – 104, 1999. ISSN 0168-583X. doi: [http://dx.doi.org/10.1016/S0168-583X\(98\)00974-4](http://dx.doi.org/10.1016/S0168-583X(98)00974-4). URL <http://www.sciencedirect.com/science/article/pii/S0168583X98009744>.
- [20] Maarten Snee and Wim Ubachs. Direct measurement of the rayleigh scattering cross section in various gases. *Journal of Quantitative Spectroscopy and Radiative Transfer*, 2005.
- [21] C. P. Achenbach and J. H. Cobb. Computational studies of light acceptance and propagation in straight and curved multimodal active fibres. *J. Opt. A: Pure Appl. Opt.*, 2003.
- [22] Axel Kuonen. Characterisation of the hamamatsu mppc multichannel array for lhcb scifi tracker v.12.2015. Technical report, EPFL Lausanne, 2016.
- [23] W. Demtröder. *Experimentalphysik 3: Atome, Moleküle und Festkörper*. Springer, 2005.

- [24] B. Leverington. Lhcb scintillating fibre tracker: Test beam report 2015. Technical Report LHCb-PUB-2015-025, June 2016.
- [25] Axel Kuonen. Characterisation of the hamamatsu mppc multichannel array for lhcb scifi tracker v.12.2015. Technical report, EPFL Lausanne, 2016.
- [26] Stéphane Callier, Christophe Dela Taille, Gisèle Martin-Chassard, and Ludovic Raux. EASIROC, an Easy & Versatile ReadOut Device for SiPM. *Phys. Procedia*, 37:1569–1576, 2012. doi: 10.1016/j.phpro.2012.02.486.
- [27] The LHCb Scintillating Fibre Tracker Collaboration. Lhcb scintillating fibre tracker: Test beam report 2015. Technical Report LHCb-PUB-2015-025, 2016.
- [28] Blake Leverington. Schematic of scintillating pad trigger. Private Communication, 2016.
- [29] Lukas Witola. Commissioning of a test stand for quality assurance of fibre modules using cosmic rays for the scifi detector upgrade, 2016.
- [30] W. Demtröder. *Experimentalphysik 4: Kern-, Teilchen- und Astrophysik*. Springer, 2014.
- [31] Sebastian Bachmann. Fp13 - measurement of muon properties, 2013.
- [32] S. Bruggisser. Literature study on the radiation damage on kuraray scsf-78m and scsf-78mj fibers. *LHCb TWiki*, 2012. URL <https://twiki.cern.ch/twiki/pub/LHCb/ScintFiber/FiberSummaryNew.pdf>.
- [33] C. Zorn. A pedestrian’s guide to radiation damage in plastic scintillators. *Radiation Physics and Chemistry*, 41(1–2):37 – 43, 1993. ISSN 0969-806X. doi: [http://dx.doi.org/10.1016/0969-806X\(93\)90040-2](http://dx.doi.org/10.1016/0969-806X(93)90040-2). URL [//www.sciencedirect.com/science/article/pii/0969806X93900402](http://www.sciencedirect.com/science/article/pii/0969806X93900402).
- [34] Ana Barbara Rodrigues Cavalcante, Laura Gavardi, Maurice Glaser, Christian Joram, Matthias Karacson, and Robert Kristic. Irradiation of a 2.5 m long SciFi module with 24 GeV/c protons to the dose profile expected in LHCb. Technical Report LHCb-PUB-2016-001. CERN-LHCb-PUB-2016-001, CERN, Geneva, Jan 2016. URL <https://cds.cern.ch/record/2120729>.
- [35] Laura Gavardi. Private communication, September 2016.

Erklärung:

Ich versichere, dass ich diese Arbeit selbstständig verfasst habe und keine anderen als die angegebenen Quellen und Hilfsmittel benutzt habe.

Heidelberg, den 01. Februar 2017

.....